Numerical Study of the Receptivity of a Blunt Cone to Hypersonic Freestream Pulse Disturbances

Simon He* and Xiaolin Zhong†
University of California, Los Angeles, California, 90095, USA

While receptivity plays a key role in the transition of hypersonic flows, most prior computational receptivity studies have neglected to replicate broadband frequency disturbances. This work uses perfect gas Linear Stability Theory (LST) and Direct Numerical Simulation (DNS) to study the receptivity of flow over a 5.080 mm nose radius straight cone at Mach 10 using finite spherical pulses to approximate disturbances with broadband frequency spectra. Freestream fast acoustic, slow acoustic, temperature, and vorticity pulses were studied to investigate a wide range of forcing conditions. Unsteady DNS predicts second mode growth and agrees well with LST. DNS and LST data are used to extract second mode receptivity coefficients and phase spectra. Preliminary results for the 5.080 mm case show that the strongest second mode receptivity response was seen for the finite spherical temperature pulse, followed by the finite fast acoustic, slow acoustic, and vorticity pulses in that order. Spectral phase coefficients corresponding to the receptivity magnitude coefficients were also found and showed excellent agreement between the finite pulse cases at higher second mode frequencies. Lower disturbance frequencies demonstrate potential differences in the receptivity mechanisms between the temperature pulse and the acoustic and vorticity pulses.

I. Introduction

The accurate prediction of laminar to turbulent transition in hypersonic flows is a major concern when using computational fluid dynamics (CFD) to aid in the design of high-speed vehicles. Transition to turbulence is known to dramatically increase aerodynamic drag and heating on the vehicle's surface and significantly affect the control of the vehicle [1–3]. Delaying transition and accurately predicting its behavior in hypersonic vehicles will allow for greater specificity in the design of thermal protection systems (TPS) to minimize their weight impact. Doing so would have a substantial payoff, enabling better flight performance and expanded payload capacities for potential hypersonic vehicles.

Transition in a hypersonic boundary layer is governed by several mechanisms, and in the case of weak environmental forcing can be broken down into three distinct stages: (i) boundary layer receptivity, (ii) linear growth of small amplitude disturbances, and (iii) nonlinear breakdown at finite disturbance amplitudes [4]. Traditionally, studies on hypersonic boundary layer transition at zero angle of attack have focused on the linear growth of Mack modes, for which the second mode instability has been found to dominate [5]. Receptivity mechanisms dictate the initial disturbance amplitudes of flow instabilities, such as the second mode, in response to external forcing. This external forcing can come in the form of surface or freestream disturbances, as depicted in the schematic diagram shown in Fig. 1. These initial amplitudes can greatly impact the general stability behavior of the flow[6]. Studies of receptivity commonly focus on the response to freestream noise which, for compressible flows, can be categorized into three distinct types: acoustic, entropy, and vorticity disturbances[7]. In hypersonic flows, the interaction of freestream disturbances of any of these categories with the bow shock generates disturbance waves of all three types that can perturb the boundary layer[8]. However, the mechanisms of the shock-disturbance interactions for each of these freestream disturbances can vary and cause differences in the resulting disturbance content, both in terms of wave amplitude and phase[9]. Thus, a wide-ranging consideration of all the disturbance types with realistic continuous frequency spectra is needed to fully characterize the receptivity of a hypersonic flow.

The receptivity of hypersonic boundary layers to freestream disturbances has been extensively studied in flows over flat plates[4, 10–15]. In their computational studies Ma and Zhong [4, 11, 12] found that freestream acoustic disturbances generate initially stable modes near the leading edge of their flat plate, which then become unstable after synchronization. Synchronization occurs when the discrete modes (described by Mack as the multiple-viscous solutions[16]) originating from the continuous freestream fast and slow acoustic spectra interact and exchange energy.

*Ph.D. Candidate, Mechanical and Aerospace Engineering Department, simon.he.ucla@gmail.com, AIAA Student Member.
†Professor, Mechanical and Aerospace Engineering Department, xiaolin@seas.ucla.edu, AIAA Associate Fellow.

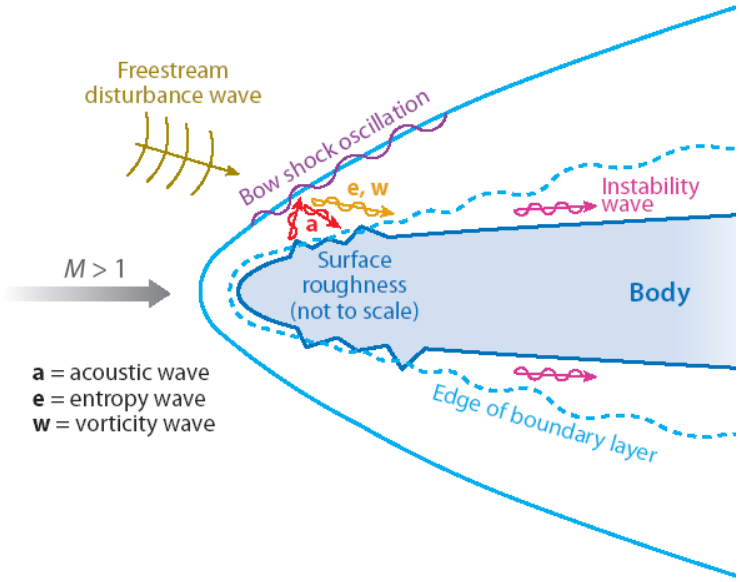

Fig. 1 Schematic diagram depicting general receptivity pathways, adapted from Zhong and Wang[3].

This exchange can eventually destabilize one of the discrete modes and cause an amplifying Mack mode instability. In their studies, Ma and Zhong[4] found that freestream acoustic, vorticity, and entropy waves modelled as discrete frequency Fourier modes could all excite discrete mode disturbances in flat plate boundary layers, though the receptivity mechanisms differed greatly between the disturbance types. They showed that a freestream entropy disturbance excited strong stable mode I (F1) disturbances upstream on the plate that would then be converted into mode II (F2) mode instabilities after synchronization. The freestream fast acoustic disturbance similarly excited mode I (F1) and mode II (F2) disturbances. However, stronger oscillations which were indicative of much more substantial multimodal coupling were observed for the fast acoustic case. The slow acoustic disturbance was instead shown to successfully excite an unstable second mode, which was found to be what is now known as the discrete mode S, downstream of synchronization. Malik and Balakumar[13] similarly found that planar, discrete frequency slow acoustic waves impinging on a flat plate generated much stronger receptivity responses compared to other disturbances and that leading-edge bluntness seemed to stabilize the boundary layer. The mode F and mode S terminology discussed here were recently coined by Fedorov and Tumin to more directly reflect the asymptotic behavior of the discrete modes, and is discussed in detail in[17]. The results of these studies indicate diffierent receptivity paths for different disturbance types, and necessitate a wide-ranging consideration of disturbances in order to fully characterize the receptivity response of a flow.

Numerous studies have also been made on the receptivity of cone geometries to freestream disturbances[18–23]. Zhong and Ma[18] investigated the receptivity of a blunt cone with discrete frequency freestream fast acoustic waves at Mach 7.99. They found through LST that the unstable second mode for this case was mode S, similar to their previous flat plate case [4]. Contrary to their previous flat plate result, the fast acoustic disturbance was also found to excite the second mode instability in the boundary layer for the cone. This indicated that the receptivity process differed significantly between these two geometries, which can be attributed to flow features such as bow shock interactions, nose bluntness, and potential entropy layer instabilities. Similarly, Balakumar and Kegerise [19, 20] found that both discrete frequency vorticity and acoustic disturbances could similarly excite second mode instabilities in cone flows, and that the receptivity response was stronger for acoustic disturbance waves. They also reported that wave incidence had some effect on the receptivity response, indicating a need to account for more complex disturbance conditions to fully approximate the envelope of conditions found in flight. Kara et al.[22] used receptivity simulations for discrete frequency acoustic waves to predict transition on sharp and blunt cones. They found that while freestream acoustic waves readily generated second mode instabilities downstream on the cone, second mode amplification was unable to accurately predict the transition behavior observed in large nose bluntness cones. Possible explanations for this include non-modal disturbance growth from sources like transient growth[24], or a failure to accurately capture the effects of freestream environmental noise in the disturbance model[25].

Many past receptivity studies utilized planar freestream disturbances modelled as discrete frequency Fourier modes[4, 20]. However, this overly simplified model ignores the complex forcing environments generated by broadband disturbances and inaccurately attributes the energy of the forcing to only the most amplified frequency[21]. Balakumar and Chou[21] approximated these broadband frequency disturbances through carefully chosen combinations of discrete frequency, two-dimensional planar slow acoustic waves which were imposed simultaneously on the flow. The amplitude of each disturbance wave in the packet was determined by equating the energy of each discrete wave with a chosen frequency bin in the experimentally measured freestream noise spectrum. Through this method they were able to calculate second mode receptivity coefficients, defined as the normalized surface pressure disturbance at the neutral point, for a variety of sharp and blunt cone cases. They found that receptivity coefficients decreased with nose bluntness and that the new receptivity data allowed for fairly accurate transition prediction for their sharp nose cases using a surface pressure threshold criterion. However, the accuracy of the threshold criterion they used decreased significantly for blunter cones.

Huang and Zhong [9, 26] instead modeled a broadband disturbance through the use of a finite axisymmetric freestream hotspot, which was equivalent to an entropy disturbance, over a compression cone. They showed that this hotspot was effective in exciting second mode instabilities in the boundary layer. They also found that the resulting disturbance growth rate and phase speed compared well to LST, and corroborated the results from the experimental studies at Purdue by Wheaton et al.[27] and Chou et al.[28, 29] that the simulations were based on. The receptivity mechanism for the entropy spot over a compression cone was found to be very similar to that of discrete acoustic waves over a blunt cone, but different from entropy spot disturbances for flat plates. This further reinforces the significance of geometry for receptivity mechanisms. They were then able to use a combination of the unsteady DNS and the LST disturbance data to extract both spectral receptivity coefficients for the second mode, and the phase angle spectra of the boundary layer disturbance. With these results, the full response to this particular temperature disturbance as well as other arbitrary axisymmetric temperature disturbances can be reconstructed[9, 23]. While these studies showed that Gaussian pulses could successfully approximate continuous frequency spectrum disturbances and excite significant modal instabilities in hypersonic flows over cones, they were very limited in terms of the disturbance types they considered. Additional acoustic and vorticity disturbances must also be investigated to account for the differences in receptivity mechanisms between disturbance types.

The most direct application of receptivity data is in the development of improved transition estimation methods. LST has historically been used to track the spatial and temporal development of discrete instability modes, though parabolized stability equations (PSE) have also risen in prominence recently to account for nonparallel and nonlinear effects[30]. Current transition prediction procedures, such as the e^N method, rely on using modal instability growth rates derived from LST or PSE to determine the relative amplification of boundary layer disturbances. Empirically determined threshold values are then used to predict the onset of turbulent transition[21, 31, 32]. This prediction approach assumes that relative amplification is the most critical factor in determining transition and often ignores the initial disturbance amplitudes generated by receptivity. While this assumption can provide good internal consistency in a given experimental environment, transition thresholds based on this methodology can vary significantly between different experiments. Schneider[6] described similar experiments with threshold N-factors of 5 and 8, demonstrating the potential impact of environmental noise on transition. Variability of this degree prevents the widespread application of uncorrected prediction results between experiments.

A number of improved transition prediction methodologies have been proposed to overcome the limitations of the traditional e^N method. Crouch[31] proposed a variable N-factor method that fits a variation of the N-factor with a simplified model of the freestream response. This has the advantage of requiring no additional computations after the disturbance response and linear growth (N-factor) data are first obtained. Another improved transition model is based on the amplitude method proposed by Mack[33], which also uses experimental receptivity data to correlate initial disturbance amplitudes to freestream noise environments. Marineau[34] used this amplitude method, empirical receptivity correlations, and simulation results in an iterative process to estimate transition on a selection of sharp and blunt nosed cones. He showed that this method could predict transition for blunt cones and cones at angles of attack much more accurately than more traditional e^N methods. Ustinov[35] also extended this amplitude method to investigate laminar-turbulent transition on a swept wing using a combined amplitude criterion for steady state and time dependent perturbations in the flow and found that this method successfully reproduced experimentally observed dependencies on Reynolds number, local surface roughness, and freestream turbulence. The receptivity results applied in Crouch's and Marineau's studies used highly empirical receptivity correlations. Utilizing receptivity spectra derived from DNS simulations would provide significantly improved precision and potentially help further improve the accuracy of these alternative transition prediction methods.

The current study presents a consideration of multiple disturbance types in order to generate a more complete view of the receptivity response of a blunt cone to broadband frequency freestream pulse disturbances and continues in the same vein as previous work by the group[36]. The receptivity mechanisms for a finite, spherical pulse geometry are investigated in particular here to compare against previous results for a blunter cone case. Broadband freestream fast acoustic, slow acoustic, temperature, and vorticity disturbances are modelled using gaussian pulses. The meanflow geometry is based on experiments by Marineau et al.[37] for Mach 10 flow over a 5.080 mm nose radius cone from the AEDC windtunnel 9. The numerical study in this paper consists of three primary components: (1) the steady meanflow simulation and LST analysis, (2) the unsteady DNS simulation using the freestream pulse disturbances, and (3) the generation of the spectral receptivity coefficients and phase angles using the LST and unsteady DNS results.

II. Simulation Conditions

This investigation focuses on a cone geometry and freestream conditions derived from Marineau et al.'s[37] experiments. The steady meanflow in this study is referred to as Case I and is a 5.080 mm nose radius straight cone based on run 3746 in Marineau et al.'s study. The steady and unsteady cases were studied at 0 angle of attack. The case was chosen due to the detailed transition data provided by Marineau and for direct comparison to results for similar cases studied previously [36].

The cone geometry for Case I is 1.5 m in length along the central line of symmetry. The DNS simulations used 240 points in the wall-normal direction and roughly five points per millimeter on the surface of the cone in the streamwise direction. Four points are used in the periodic spanwise direction, though only one point is directly calculated at each timestep utilizing a spectral collocation method. The flow conditions for this study are summarized in Table 1

Table 1 Freestream flow conditions for DNS simulations.

$R_n\ (mm)$	M_∞	$h_{0,\infty}\ (MJ/kg)$	$\rho_\infty\ (kg/m^3)$	$p_\infty\ (kPa)$	$T_\infty\ (K)$	$U_\infty\ (m/s)$	$T_w/T_{0,\infty}$	Pr	$Re/m\ (1E6/m)$
5.080	9.81	1.06	0.0422	0.64	50.8	1425	0.3	0.72	19.11

The unsteady cases here are differentiated by their freestream disturbance type. These cases are listed and labelled for more concise reference in Table 2 below for Case I. The details of the pulse geometries and freestream disturbance formulations are given in section VI.A.

The DNS code used in this study utilizes a shock-fitting formulation with the parameters in Table 1 defining the freestream conditions upstream of the shock formed over the body. Marineau et al.[37] used curve fits of experimental data to generate the viscosity used for the Reynolds number calculations instead of Sutherland's Law. This lead to approximately a 15% increase in the calculated freestream unit Reynolds numbers between this study and Marineau's.

III. Governing Equations

The solution methods for the DNS and LST codes were originally developed and implemented by Zhong and Ma [4, 38] and are formulated for a perfect gas. This assumption was made based on the low freestream stagnation enthalpy reported in Table 1. Their formulation is highlighted here for clarity. The three-dimensional Navier-Stokes equations in conservative form consist of a single species mass conservation equation, three momentum conservation equations, and

Table 2 Freestream disturbance cases for unsteady DNS.

Disturbance Type	Case I
Finite Spherical Fast Acoustic	I1
Finite Spherical Slow Acoustic	I2
Finite Spherical Temperature	I3
Finite Spherical Vorticity	I4

the energy equation. The governing equations in vector form are written as

$$\frac{\partial U}{\partial t} + \frac{\partial F_j}{\partial x_j} + \frac{\partial G_j}{\partial x_j} = 0, \quad (j = 1, 2, 3) \tag{1}$$

where U is the state vector of conserved quantities and F_j and G_j are the inviscid and viscous flux vectors, respectively. Here, the j indices indicate Cartesian coordinates in the streamwise, radial, and azimuthal directions about the cone. The conservative vector U is comprised of five conservative flow variables for mass, momentum, and energy:

$$U = \begin{bmatrix} \rho & \rho u_1 & \rho u_2 & \rho u_3 & e \end{bmatrix}^T \tag{2}$$

Additionally, the inviscid F_j and viscous G_j flux vectors are written as:

$$F_j = \begin{bmatrix} \rho u_j \\ \rho u_1 u_j + p\delta_{1j} \\ \rho u_2 u_j + p\delta_{2j} \\ \rho u_3 u_j + p\delta_{3j} \\ (e + p)u_j \end{bmatrix} \tag{3}$$

$$G_j = \begin{bmatrix} 0 \\ \tau_{1j} \\ \tau_{2j} \\ \tau_{3j} \\ \tau_{jk}u_k - q_j \end{bmatrix} \tag{4}$$

Since this study assumes a perfect gas flow, the equation of state and the transport equations are

$$p = \rho RT \tag{5}$$

$$e = \rho(C_v T + \frac{1}{2}u_k u_k) \tag{6}$$

$$\tau_{ij} = \mu(\frac{\partial u_i}{\partial x_j} + \frac{\partial u_j}{\partial x_i}) - \lambda \frac{\partial u_k}{\partial x_k}\delta_{ij} \tag{7}$$

$$q_j = -\kappa \frac{\partial T}{\partial x_j} \tag{8}$$

Furthermore, the viscosity coefficent μ is calculated through Sutherland's law for nitrogen gas

$$\mu = \mu_r \left(\frac{T}{T_0}\right)^{\frac{3}{2}} \frac{T_r + T_s}{T + T_s} \tag{9}$$

In these equations R is the gas constant while c_p and c_v are the specific heats, which are assumed to be constant for a given ratio of specific heats γ. Here, the environment is assumed to be composed entirely of diatomic nitrogen which results in $\gamma = 1.4$. The coefficient λ is assumed to be $-2\mu/3$ and the heat conductivity coefficient κ is computed through a fixed Prandtl number of 0.72.

IV. DNS

The DNS code utilizes a high-order shock-fitting method for a perfect gas flow that was developed to compute the flow field surrounding a blunt cone moving in a hypersonic freestream. The numerical method is summarized here for clarity. First, the Navier-Stokes equations are transformed into computational space

$$\frac{1}{J}\frac{\partial U}{\partial \tau} + \frac{\partial E'}{\partial \xi} + \frac{\partial F'}{\partial \eta} + \frac{\partial G'}{\partial \zeta} + \frac{\partial E'_v}{\partial \xi} + \frac{\partial F'_v}{\partial \eta} + \frac{\partial G'_v}{\partial \zeta} + U\frac{\partial (1/J)}{\partial \tau} = 0 \tag{10}$$

where J is the Jacobian of the coordinate transformation and (ξ, η, ζ) are the transformed computational coordinates in the streamwise, radial, and azimuthal directions of the cone. The original curvilinear coordinates of the grid are converted using a coordinate transformation in order to better facilitate the application of high-order finite difference stencils. This transformation is given in Eq. 11.

$$\begin{cases} \xi = \xi(x, y, z) \\ \eta = \eta(x, y, z, t) \\ \zeta = \zeta(x, y, z) \\ \tau = t \end{cases} \iff \begin{cases} x = x(\xi, \eta, \zeta, \tau) \\ y = y(\xi, \eta, \zeta, \tau) \\ z = z(\xi, \eta, \zeta, \tau) \\ t = \tau \end{cases} \tag{11}$$

The transformed fluxes in the computational coordinates are then given by

$$E' = \frac{F_1\xi_x + F_2\xi_y + F_3\xi_z}{J} \tag{12}$$

$$F' = \frac{F_1\eta_x + F_2\eta_y + F_3\eta_z}{J} \tag{13}$$

$$G' = \frac{F_1\zeta_x + F_2\zeta_y + F_3\zeta_z}{J} \tag{14}$$

$$E'_v = \frac{G_1\xi_x + G_2\xi_y + G_3\xi_z}{J} \tag{15}$$

$$F'_v = \frac{G_1\eta_x + G_2\eta_y + G_3\eta_z}{J} \tag{16}$$

$$G'_v = \frac{G_1\zeta_x + G_2\zeta_y + G_3\zeta_z}{J}. \tag{17}$$

A low-dissipation, fifth-order upwinded stencil is used for the inviscid fluxes while a sixth-order central stencil is used to discretize the viscous terms as shown in Eq. 18.

$$\frac{\partial f_i}{\partial x} = \frac{1}{hb_i} \sum_{k=-3}^{3} \alpha_{i+k} f_{i+k} - \frac{\alpha}{6! b_i} h^5 \left(\frac{\partial f^6}{\partial^6 x} \right) \tag{18}$$

where the coefficients α and b are defined as

$$\alpha_{i\pm3} = \pm 1 + \frac{1}{12}\alpha, \qquad \alpha_{i\pm2} = \mp 9 - \frac{1}{2}\alpha$$

$$\alpha_{i\pm1} = \pm 45 + \frac{5}{4}\alpha, \qquad \alpha_i = -\frac{5}{3}\alpha$$

$$b_i = 60$$

Here, h is the step size, $\alpha < 0$ generates an upwind explicit scheme, and $\alpha = 0$ leads to a central scheme. In this study the inviscid terms use $\alpha = -6$ for a low dissipation fifth order upwinded difference, and the viscous terms are discretized with a sixth order central scheme using $\alpha = 0$. The derivatives in the azimuthal direction are treated with Fourier collocation due to axisymmetry. To compute second derivatives, the first order derivative operator is applied twice. Flux splitting is applied with a local Lax-Friedrichs formulation, resulting in

$$F = F^+ + F^- \tag{19}$$

where the matrices $F^\pm$ are defined as

$$F^\pm = \frac{1}{2}(F \pm \Lambda U) \tag{20}$$

and Λ is a diagonal matrix that ensure that F^+ contains only positive eigenvalues and F^- contains only negative eigenvalues.

In the shock-fitting formulation the shock itself is treated as a computational boundary at

$$\eta(x, y, z, t) = \eta_{max} = constant \tag{21}$$

The flow variables behind the shock are determined through a combination of the Rankine-Hugoniot relations across the shock and a characteristic compatibility relation behind the shock. Additionally, the position $H(\xi, \zeta, \tau)$ and velocity $H_\tau(\xi, \zeta, \tau)$ of the bow shock in computational coordinates are also concurrently solved at each timestep with the other flow variables. Finally, the solution is advanced in time using a low-storage first-order Runge-Kutta method from Williamson[39]. The details of this shock-fitting formulation and the numerical methods can be found in Zhong[38].

V. LST

The linear stability analysis (LST) implementation used in this study was originally developed and verified by Ma and Zhong [4, 11, 12, 18] and then extended to study perfect gas flow over cone geometries by Lei and Zhong[25] and Huang and Zhong[9]. The LST relations are derived from the governing Navier-Stokes equations in Eq. 1 by substituting the instantaneous flow, which can be decomposed into a mean and fluctuating component:

$$q(x, y, z, t) = \overline{q}(x, y, z) + q'(x, y, z, t) \tag{22}$$

Here $q(x, y, z, t)$ is the instantaneous flow for a given dsturbance variable, $\overline{q}(x, y, z)$ is the mean component, and $q'(x, y, z, t)$ is the fluctuating component. Since the steady mean flow component is assumed to satisfy the governing equations, it can be subtracted out. The mean flow is then assumed to be both axisymmetric/2-D and quasi-parallel to reduce any remaining meanflow terms to functions of only the wall-normal coordinate y.

$$\overline{q}(x, y, z) = \overline{q}(y) \tag{23}$$

The disturbances are assumed to be small enough that they remain in the linear regime, thus quadratic and higher order perturbation terms (q') are cancelled out. The linearized governing equations can then be written in the form

$$\tilde{\Gamma}\frac{\partial q'}{\partial t} + \tilde{A}\frac{\partial q'}{\partial x} + \tilde{B}\frac{\partial q'}{\partial y} + \tilde{C}\frac{\partial q'}{\partial z} + \tilde{D}q' + \tilde{V}_{xx}\frac{\partial^2 q'}{\partial x^2} + \tilde{V}_{yy}\frac{\partial^2 q'}{\partial y^2} + \tilde{V}_{zz}\frac{\partial^2 q'}{\partial z^2} + \tilde{V}_{xy}\frac{\partial^2 q'}{\partial x \partial y} + \tilde{V}_{xz}\frac{\partial^2 q'}{\partial x \partial z} + \tilde{V}_{yz}\frac{\partial^2 q'}{\partial y \partial z} = 0 \tag{24}$$

The system is further simplified by the introduction of a normal mode solution $q' = \hat{q}(y)\exp\left[i\left(\alpha x + \beta z - \omega t\right)\right]$, where ω is the circular frequency of the disturbance and α and β are the spatial wavenumbers of the x streamwise and z spanwise coordinates respectively. In this study a 2-D spatial stability approach is used. For the spatial stability approach the circular frequency of a disturbance mode, ω^* defined as $\omega = 2\pi f$, must be manually set to be a real number while β is set to 0 for a two dimensional disturbance. This ω is based on the disturbance frequency being studied. In this case α is complex which results in the dispersion relation $\alpha = \Omega(\omega, \beta)$. The complex spatial wavenumber α can be written as $\alpha = \alpha_r + i\alpha_i$. Here, $-\alpha_i$ is the growth rate of the disturbance. The problem is now reduced to a coupled set of 5 ordinary differential equations

$$\left(\mathbf{A}\frac{d^2}{dy^2} + \mathbf{B}\frac{d}{dy} + \mathbf{C}\right)\vec{\phi} = \vec{0}. \tag{25}$$

where $\vec{\phi} = \left[\hat{u}, \hat{v}, \hat{P}, \hat{T}, \hat{w}\right]^T$ comprises the eigenfunctions of the system and $\mathbf{A}$, $\mathbf{B}$ and $\mathbf{C}$ are complex square matrices of size 5. This is now a boundary value problem where the derivative operators can be discretized and the equations solved numerically. The system of equations is solved using using a multi-domain spectral method and boundary conditions similar to Malik[40] which allows for clustering of points near domains of interest.

The wavenumber results from spatial LST can be used to derive the characteristic phase speed of a disturbance. The nondimensional phase speed of a disturbance is defined from LST as

$$c_r = \frac{(\omega^*/U^*_\infty)}{\sqrt{\beta^2 + \alpha_r^2}} \tag{26}$$

which, for a two-dimensional disturbance, can be reduced to

$$c_r = \frac{(\omega^*/U^*_\infty)}{\alpha_r} \tag{27}$$

This phase speed is non-dimensionalized by the characteristic freestream velocity. The results of spatial LST can be further nondimensionalized using the local Reynolds number R for streamwise position and a non-dimensional frequency F. These are quantities are defined as:

$$R = Re_x^{1/2} = \sqrt{\frac{\rho_\infty^* U_\infty^* s}{\mu_\infty^*}} = \frac{\rho_\infty^* U_\infty^* L^*}{\mu_\infty^*} \tag{28}$$

$$F = \frac{\omega^* \mu_\infty^*}{\rho_\infty^* U_\infty^{*2}} \tag{29}$$

where additional spatial nondimensionalization is performed using the local boundary layer height parameter L^*, which is based on the local streamwise position and freestream parameters.

$$L^* = \sqrt{\frac{\mu_\infty^* s^*}{\rho_\infty^* U_\infty^*}} \tag{30}$$

While LST can be used to identify both the unstable disturbance frequencies and their growth rates, it does not directly specify the exact amplitude of the disturbance. Conventionally, boundary-layer transition is estimated using LST through an amplification criterion known as the e^N or the N-factor method. The N-factor is given by:

$$e^{N(s,f)} = \frac{A(s,f)}{A_0(f)} = \exp\left[\int_{s_0}^{s} -\alpha_i(s,f)ds\right] \tag{31}$$

Here $A(s,f)$ is the integrated disturbance amplitude, $A_0(f)$ is the initial disturbance amplitude, s_0 is the location where the disturbance first becomes unstable at the branch I neutral point, and $-\alpha_i$ is the spatial amplificatifon rate obtained from LST. The integration is performed for a constant frequency f, and is done numerically using trapezoidal integration. Note that $-\alpha_i > 0$ results in disturbance growth while $-\alpha_i < 0$ results in disturbance decay. The N-factor is specifically the exponent of e^N. In-flight transition N-factors are commonly understood to be between 5 and 10. However, this transition N-factor seems to hold only for sharp cones. Lei and Zhong[25], Aleksandrova et al.[41], and Balakumar and Chou[21] found that N-factors decreased considerably at similar streamwise locations for blunter cones. Marineau et al. [37] also found that blunt nose N-factors calculated at the beginning of transition were significantly lower than those for sharp nose cases, reaching as low as 0.5. Pure considerations of the N-factor are observed to be insufficient to reliably determine transition throughout a wide variety of conditions.

VI. Freestream Disturbance Model

A. Freestream Disturbance Model

The stability of the system is also studied by perturbing the meanflow and tracking the development of the boundary layer disturbances using DNS. Here, the flow is disturbed with freestream fast acoustic, slow acoustic, temperature, and vorticity disturbances in the form of Gaussian pulses. Two pulse geometries, a finite spherical and a planar pulse distribution, were utilized in this work. Since the shock is treated as a computational boundary in the simulations, these pulses can be represented analytically in the freestream. A schematic of the unsteady simulation is given for the finite pulse case in Fig. 2. The finite spherical pulse is, as its name implies, a pulse disturbance that is limited spatially in x,y, and z. The pulse disturbance distribution is given in Eq. 32. The pulse is advected by the freestream velocity along the central symmetry line of the cone. The limited scope of the finite spherical pulses causes them to only interact with cone near the nose region. The design of the pulses are based on previous work by Huang and Zhong[9] and Lei and Zhong[23].

$$q(x,y,z,t) = |q'|_\infty exp\left(-\frac{(R_c)^2}{2\sigma^2}\right) + q_\infty \tag{32}$$

The ϵM_∞ term governs the relative peak disturbance amplitude of the freestream pulse and was chosen to ensure that boundary layer disturbances remained linear. Since the receptivity response to the planar pulses was expected to be much stronger than that for the finite spherical pulses, the amplitude parameter ϵM_∞ was reduced for these cases. This ϵM_∞ term is included in $|q'|_\infty$ in Eq. 32 which is further detailed in the dispersion relations in Eq. 34, Eq. 35, Eq. 36,

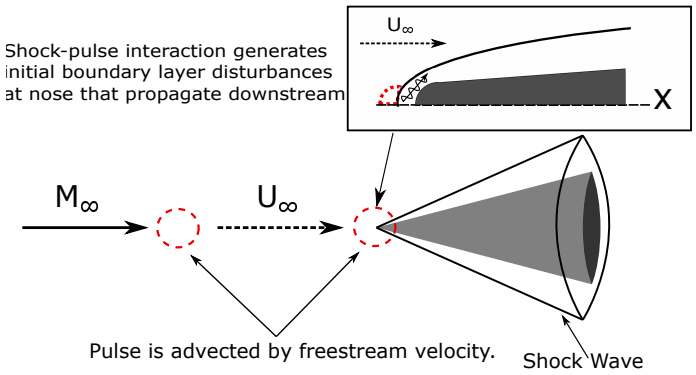

Fig. 2 Schematic diagram of unsteady simulation setup for a finite, spherical pulse disturbance in the freestream.

Table 3 Gaussian pulse parameters for DNS.

Pulse Geometry	ϵM_∞	σ	x_0
Finite Spherical	$1E-6$	$1E-3$	$-0.02m$

and Eq. 37 for the fast acoustic, slow acoustic, temperature, and vorticity disturbances respectively. The term σ controls the width of the pulse and also determines the frequency content of the disturbance. This pulse width parameter was chosen to encompass significant freestream disturbances at frequencies up to 600 kHz in order to ensure the excitation of the primary modal instabilities predicted by LST and resulted in a pulse radius of approximately 3 mm. R_c refers to the radial distance from the center of the pulse to a point (x, y, z) in the flow field. For a finite spherical pulse R_c is defined in Eq. 33.

$$R_c = \sqrt{(x - x_{pulse})^2 + (y - y_{pulse})^2 + (z - z_{pulse})^2} \tag{33}$$

Here, $(x_{pulse}, y_{pulse}, z_{pulse})$ denote the location of the pulse center. For the finite spherical pulses $y_{pulse} = z_{pulse} = 0$ is fixed. The pulse is advected in the streamwise direction by $x_{pulse} = x_0 + C_\infty t$ where C_∞ is the disturbance speed in the freestream. These speeds are defined as $C_\infty = U_\infty + a_\infty$ for fast acoustic disturbances, $C_\infty = U_\infty - a_\infty$ for slow acoustic disturbances, and $C_\infty = U_\infty$ for entropy/vorticity disturbances. Here U_∞ is the freestream velocity and a_∞ is the freestream speed of sound. In order to ensure that the same frequency spectra is shared among the disturbances, the pulse width term σ must be scaled by $1 + 1/M_\infty$ for a fast acoustic disturbance and by $1 - 1/M_\infty$ for a slow acoustic disturbance.

The coefficient q corresponds to any perturbation variable in the freestream and q' is the peak perturbation amplitude of each of these variables normalized by the freestream value. In the case of a fast acoustic disturbance, the freestream disturbance amplitudes follow the dispersion relations given by[42]:

$$|\rho'|_\infty = \frac{|P'|_\infty}{\gamma} = |u'|_\infty M_\infty = \epsilon M_\infty, \quad |s'|_\infty = |v'|_\infty = 0 \tag{34}$$

A slow acoustic disturbance in the freestream is governed by a very similar dispersion relation:

$$|\rho'|_\infty = \frac{|P'|_\infty}{\gamma} = -|u'|_\infty M_\infty = \epsilon M_\infty, \quad |s'|_\infty = |v'|_\infty = 0 \tag{35}$$

A freestream entropy disturbance is described by:

$$|\rho'|_\infty = -|s'|_\infty = \epsilon M_\infty, \quad |u'|_\infty = |v'|_\infty = |p'|_\infty = 0 \tag{36}$$

And a freestream vorticity disturbance is described by:

$$|v'|_\infty M_\infty = \epsilon M_\infty, \quad |u'|_\infty = |p'|_\infty = |s'|_\infty = 0 \tag{37}$$

Due to the calorically perfect gas assumed in this study's numerical models, the temperature disturbances can be directly related to freestream entropy disturbances by the equation of state for a perfect gas.

The parameters given in Table 3 for the finite spherical cases result in the disturbance distribution shown in Fig. 3 and can be tuned accordingly to generate different spectral amplitude distributions.

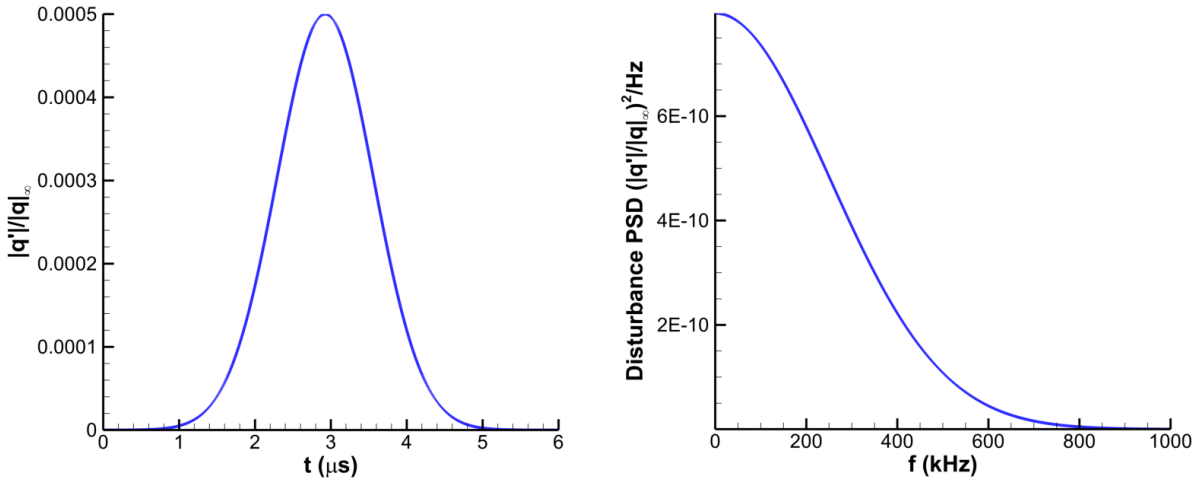

(a) (b)

Fig. 3 Freestream disturbance distributed over (a) time and (b) frequency for axisymmetric pulse.

VII. Boundary Layer Receptivity

The pulse disturbances imposed onto the cone in the unsteady simulations were chosen to induce broadband frequency perturbations in the boundary layer of the cone. In order to study the evolution of discrete frequency disturbances and correlate the unsteady DNS results with LST, the unsteady DNS is decomposed into its constituent frequency components. This was done using Fourier spectral analysis.

The time-dependent perturbation variables can be expressed in terms of their Fourier spectral components, obtained through a Fast Fourier Transform (FFT):

$$h(t_k) \equiv h_k \approx \sum_{n=0}^{N-1} H(f_n) e^{-2\pi i f_n t_k} \tag{38}$$

where $H(f_n)$ is the Fourier coefficient corresponding to the nth discretized frequency f_n . Additionally, N corresponds to the total number of Fourier collocation points used to discretize the time-dependent function $h(t)$ in Fourier space. The discretized time function h_k is defined as being the value of the time dependent function $h(t)$ at a given time $t = t_k$.

In this study, the variable $h(t)$ corresponds to local boundary-layer perturbations in the surface pressure, though other flow variables such as temperature and density may also be considered. Surface pressure was chosen since the primary instability modes in the boundary layer are expected to be acoustic in nature. The complex Fourier coefficients $H(f_n)$ represents the spectral value of the boundary layer perturbations in the frequency domain. The purely complex portion of $H(f_n)$ corresponds to the phase of the perturbation, and $|H(f_n)|$ are the perturbation amplitudes for these variables at each spectral frequency.

Since LST was used to validate the results of the unsteady DNS analysis, local growth rates and wavenumbers need to be calculated from the Fourier decomposed perturbation data. Following a similar procedure to Ma and Zhong[4] and Huang and Zhong[9], the local growth rates for each frequency are determined by

$$-\alpha_i = \frac{1}{|H(f_n)|} \frac{d|H(f_n)|}{ds} \tag{39}$$

and the local wave numbers are determined by

$$\alpha_r = \frac{d\phi_n}{ds} \tag{40}$$

where s corresponds to the local streamwise coordinates, f_n is the nth disturbance frequency of interest, and ϕ_n is the disturbance phase angle of the nth frequency. The nondimensional phase speed of a given disturbance at a given frequency is defined as

$$c_r = \frac{2\pi f_n}{U_\infty \alpha_r} \tag{41}$$

The response of the system to each freestream disturbance environment can be represented through a receptivity coefficient. This receptivity coefficient, defined here as the initial amplitude of the second mode disturbance $C_{rec}(f) = A_0(f)$, is determined using a combination of LST and unsteady DNS data. In the presence of a strong second mode it is assumed that the primary initial second mode amplitude can be extracted by inverting the amplification factor (N-factor), as shown in Eq. 42.

$$C_{rec}(f) = A_0(f) = \frac{A(s,f)}{e^{N(s,f)}} \tag{42}$$

Here $A(f)$ is the Fourier decomposed surface pressure at a given frequency normalized by the freestream disturbance and $e^N(f)$ is the exponentiated amplification factor determined through LST analysis for a given frequency f. The N-factor and perturbation data are sampled at the same streamwise position. Similarly, we derive corresponding spectral phase angles for the magnitude coefficients calculated from Eq. 42. From Eq. 40 it is known that the real wave number of a disturbance is calculated by the spatial gradient of its phase. Thus, by integrating the real wave number between two fixed spatial locations it is possible to find the expected phase change of a discrete frequency LST disturbance. In this study, these locations are the branch I neutral stability point and the sampling locations we investigated for the receptivity magnitude coefficients. This integrated LST phase change was used to attempt to extract the specific second mode phase coefficients corresponding to the magnitude coefficients discussed previously at the branch I neutral point. It is observed later that the choice of sampling location does have some influence on the resulting receptivity coefficients.

VIII. Steady Flow Field Solution

A. Case I

The steady DNS pressure and temperature meanflow contours for Case I are shown in Fig. 4a at the nose and near the beginning of the cone frustum. Fig. 4b presents the grids used at this location. Similarly to the 9.525 mm nose radius cone in our previous work [36], a total of 240 points were used in the η direction and approximately 5 points per mm were used in the ξ direction. These distributions were chosen to resolve high frequency and wavenumber disturbances and to provide sufficient resolution in the meanflow data so as to reduce numerical inconsistencies in the LST analysis. A total of 7,290 points were used in the ξ direction to resolve the cone to 1.5 m.

The meanflow pressure and temperature contours for the full cone are shown in Fig. 5.An entropy layer is seen to emerge in the nose region in Fig. 4a. The boundary and entropy layers can be visualized more clearly using wall-normal profiles of velocity and entropy. These are presented Fig. 6 at a selection of different streamwise positions. The boundary layer velocity profile in Fig. 6a demonstrates very little change in general shape or thickness throughout the downstream regions of the cone and shows that the locally parallel assumption holds for the purposes of LST. The entropy profiles in Fig. 6b show a significant entropy layer that does not merge with the boundary layer until a point that is approximately 100 nose radii downstream on the cone, and matches the results for a similar case from Balakumar and Chou[21].

The convergence of the meanflow simulation for Case I is validated by comparing the current 240 point grid in the wall normal direction with a further refined 480 point result. The results of this convergence study are shown in Fig. 7 for wall normal velocity and temperature profiles at a streamwise location 246 nose radii downstream on the cone.

The nearly identical profiles in both the velocity and the temperature qualitatively indicate grid convergence. The infinity norm of the relative error was used to quantify the difference between the original and the refined result. The infinity norm based on the velocity for this case is 2.61×10^{-6}.

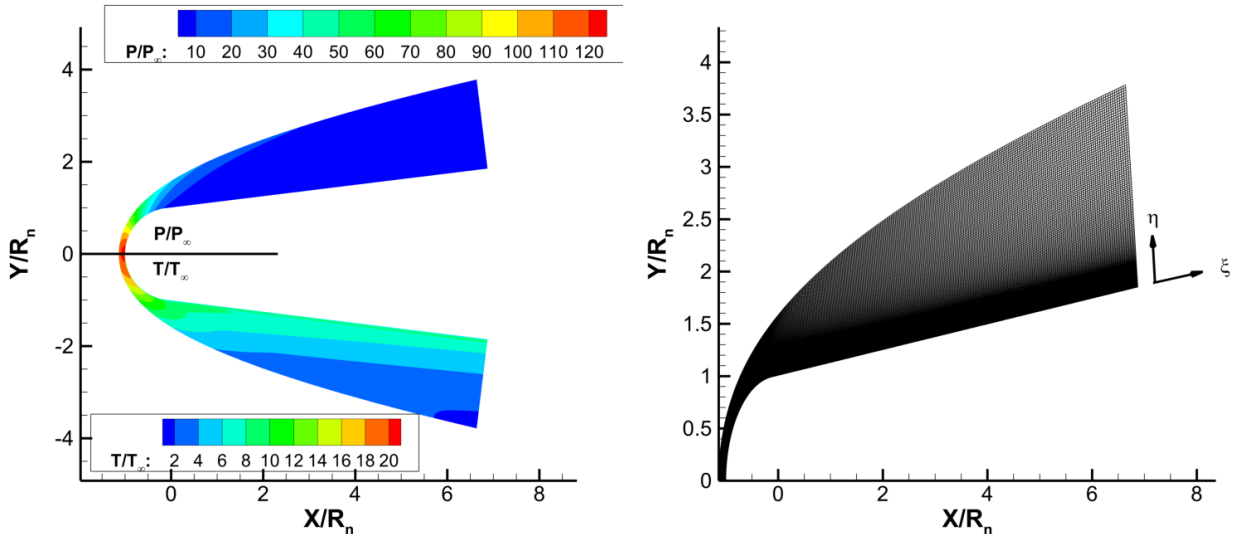

(a) (b)

Fig. 4 Partial view of (a) pressure (top) and temperature (bot) contours and (b) grids for zones 1 and 2 near nose region.

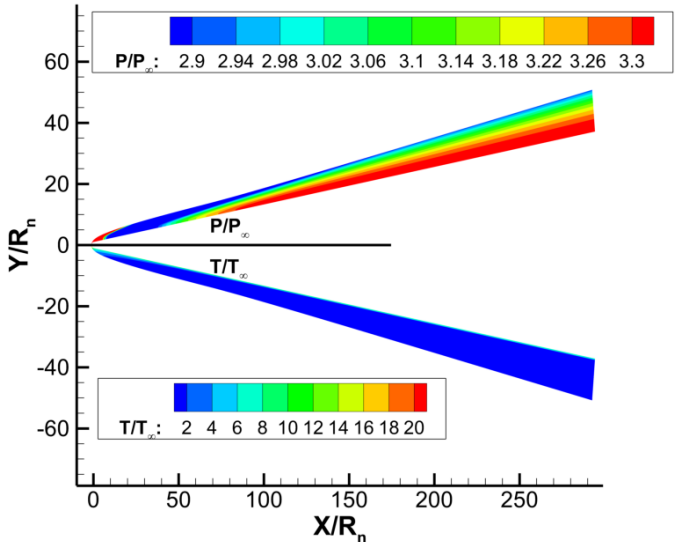

Fig. 5 Meanflow pressure (top) and temperature (bot) over the entire cone for Case I.

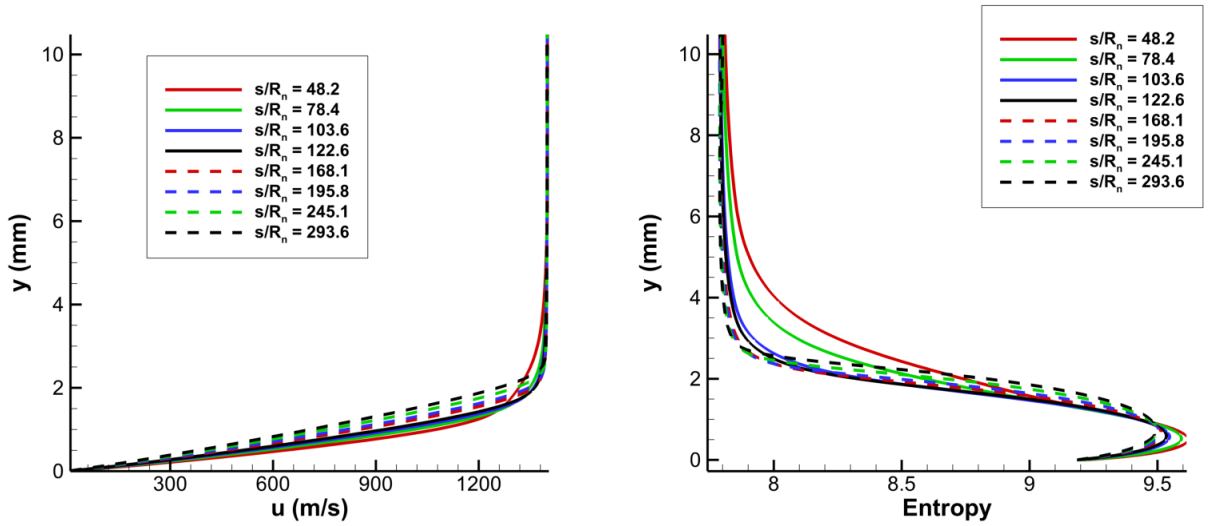

(a) (b)

Fig. 6 Wall normal (a) U velocity and (b) S entropy profiles at a selection of streamwise positions for Case I.

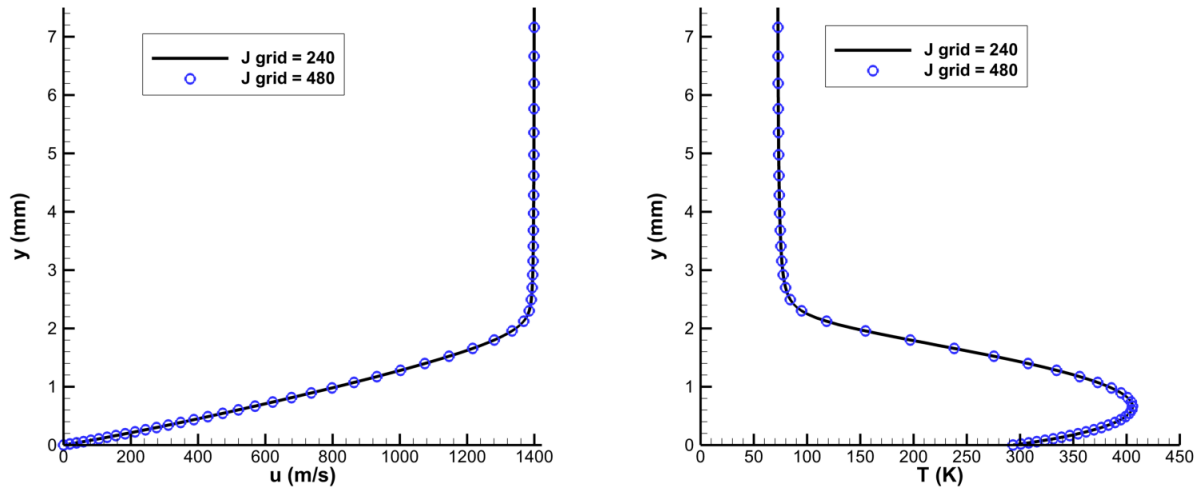

(a) (b)

Fig. 7 Grid convergence comparison of wall normal (a) U velocity and (b) T temperature profiles at $s^* = 1.25$ m for Case I, approximately 240 nose radii downstream.

IX. LST Results

LST results for Case I, the 5.080 mm nose radius cone, indicate an amplified second mode between 135 and 310 kHz. At the reported experimental transition location of 0.683 m (134 nose radii downstream on the cone), the unstable second mode is found between frequencies of 190 and 250 kHz and compares well to Marineau et al's. [37] results. The growth rate contours and the neutral stability curve are shown in Fig. 8 where $-\alpha_i > 0$ growth rates inside the curve correspond to the unstable second mode region. The neutral stability curve shown here was fitted from the branch I and branch II neutral stability points and is highlighted in black.

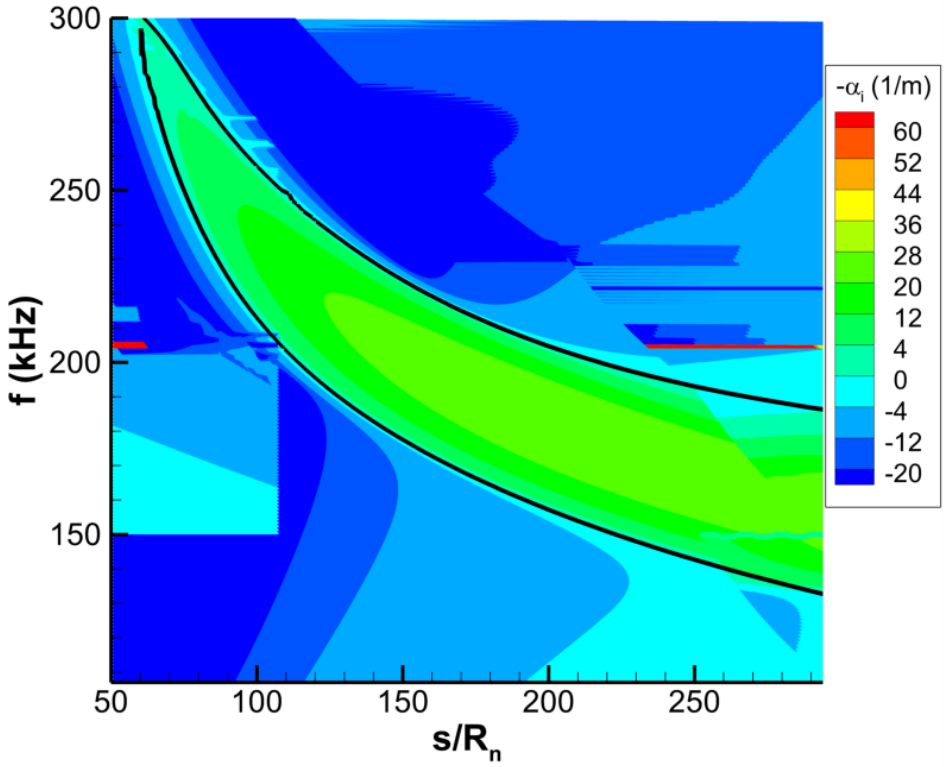

Fig. 8 LST growth rate contour and neutral stability curve up to 1.5 m or approximately 300 nose radii downstream for Case I.

The growth rates are integrated across the available data in the streamwise direction from the branch I neutral point in order to generate the N-factor curves. Fig. 9 presents N-factor curves for a subset of disturbance frequencies ranging from 150 to 260 kHz as well as a comparison of the total N-factor profile against Marineau et al.'s[37] computed results.

For this case (which corresponds to Run 3746), Marineau et al.[37] reported an experimentally determined transition location of $s = 0.683$ m approximately 134 nose radii downstream on the cone, along with a corresponding N factor of 3.7. This is over two times larger than the transition N-factor for the blunter cone studied in Case B in [36]. In general, Marineau et al.[37] found that the transition N factors of his cases scaled inversely with nose radius, as also seen in previous computational work[25, 43]. The LST results here are shown to compare well with Marineau et al.'s reported value and predict an N-factor of approximately 3.9 at this point. A direct comparison between the LST N-factors in Fig. 9a and Marineau's PSE derived N-factors are shown in Fig. 9b, in which the total profile is fitted for all of the discrete frequencies. The LST results are shown to slightly overpredict the N-factor compared to the PSE results from Marineau et al. This is again attributed to the differences in formulation between the LST used in this work and the PSE utilized by Marineau et al., namely in the nonparallel effects present upstream on the cone geometry. However, it can be seen here that these effects are relatively minor and do not significantly affect the general downstream disturbance development significantly, as can be seen in the very similar N-factor slopes between the two computational methods.

The phase speed and growth rates of the 200 kHz disturbance are presented in Fig. 10. These will again be used to

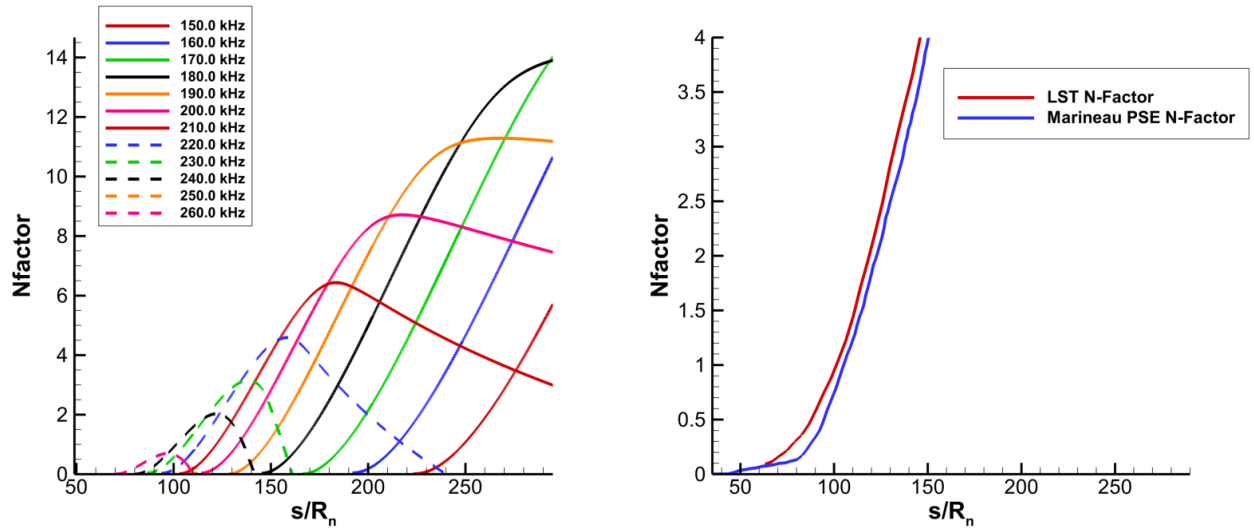

Fig. 9 (a) N-factor data ranging between 150 kHz to 260 kHz with Δf = 10 kHz. (b) Current LST N-factors vs. Marineau's[37] reported PSE N-factors.

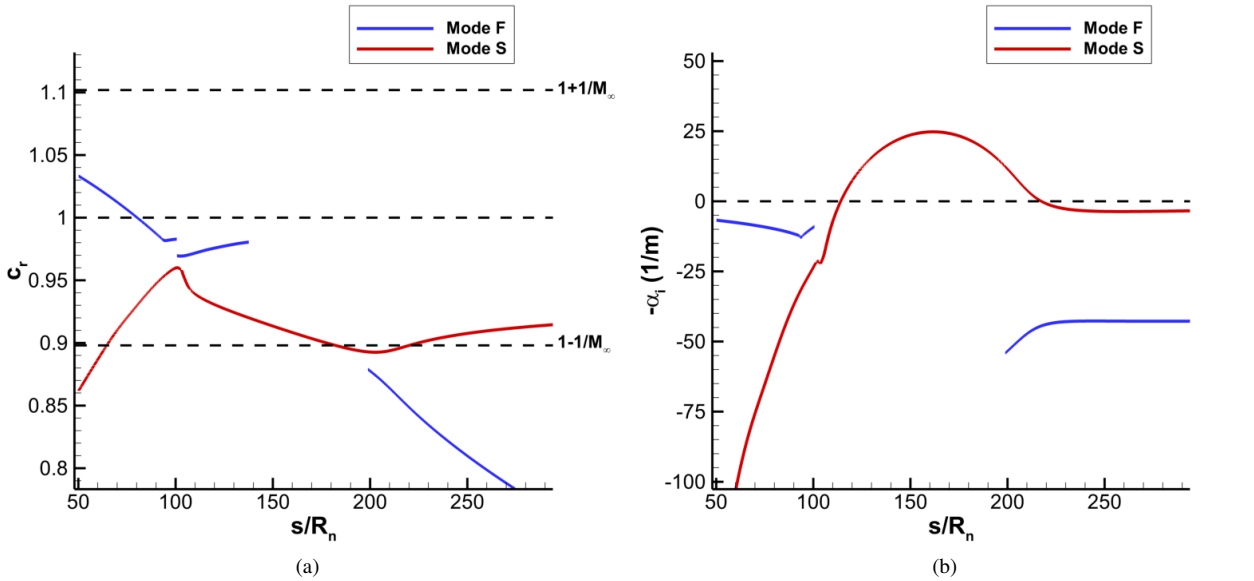

Fig. 10 Streamwise LST results at f = 200 kHz for (a) Phase Speed (b) Growth Rate for Case I.

validate the results of the unsteady DNS and to help investigate the mechanisms of receptivity in for each pulse. The 200 kHz disturbance was chosen in particular because it is expected to be highly excited, as shown in [37]. From Fig. 10b it can be seen that unlike Case B, the dimensional growth rate $-\alpha_i$ becomes positive for mode S, indicating that this discrete mode destabilizes after synchronization to become the second mode. The mode F disturbance is shown to remain strongly stable at this frequency as well, though the code was unable to capture the mode F disturbance between the initial synchronization point near $s/R_n = 100$ and the branch point of the mode F and mode S disturbances near $s/R_n = 200$ in both Fig. 10a and Fig. 10b. Between these points, the LST is dominated by the unstable mode S. Similar discontinuities have been observed in previous numerical studies from the group[44] and can be difficult to resolve

numerically.

X. Unsteady DNS Results

The receptivity of the cone was studied in response to a variety of broadband freestream disturbances with analytically continuous frequency spectra. The pulse disturbances described in section VI.A were introduced in the freestream and then allowed to advect along the central axis of symmetry in the streamwise direction over the meanflow. The resulting boundary layer disturbances on the cone's surface were studied using FFT to decompose the surface pressure perturbations into their spectral frequency components. The specific disturbance cases and their respective labels are given in Table 2. The disturbances are differentiated by both their freestream perturbation type and their geometry. The fast acoustic, slow acoustic, entropy, and vorticity disturbances are defined by the freestream dispersion relations in Eq. 34,35, 36, and 37 respectively.

A. Case I Finite Spherical Pulse Unsteady DNS Results

The results of the unsteady finite pulse perturbations for Case I, the 5.080 mm nose radius cone, are presented here. Fig. 11 shows pressure perturbation snapshots near the end of the cone for Case I1. Similar to the finite pulses in Case B, the general disturbance profiles for the finite pulses for Case I were very similar. Fig.11c depicts isolated boundary layer structures which are are indicative of a perturbation growing in accordance with Mack's second mode[4]. Fig. 11a and Fig. 11b depict shock-layer perturbations that originate from pulse-disturbance interactions upstream. These are very similar to the shock-layer disturbances observed previously for the finite pulses in Case B from our previous work [36] and contain both continuous mode disturbances excited upstream by the pulse, as well as first mode boundary layer disturbances[9]. These are much smaller in amplitude than the second mode disturbances depicted for Case I1 in Fig. 11c. The general structure of the shock layer disturbance fronts are qualitatively very similar between each of the cases, though the amplitudes of the disturbances vary between them.

Focusing on the second mode band shown in Fig. 11c we see the emergence of additional weak disturbances that seem to radiate from the boundary layer into the rest of the shock layer. This again indicates the existence of potential supersonic mode instabilities and further corroborates previous findings for Case B that show that these supersonic modes can exist in a wide variety of conditions, including low enthalpy flows. However, the acoustic radiation characteristic of these waves is extremely weak in comparison to the second mode and seem to be even weaker here than what was observed for Case B in [36].

The other three finite pulse cases show very similar general second mode structures, as well as as extensive weak supersonic modes. Furthermore, all of these cases experienced a sudden decrease in perturbation amplitude between $X/R_n = 1.35$ and $X/R_n = 268$. This is attributed to interference between the primary unstable mode S and the satellite waves of a stable supersonic mode F. This is highly similar to a result observed by Haley and Zhong[45] for low enthalpy hypersonic flow over a slender cone. The extent of this effect is unknown in terms of its impact on boundary layer transition, but it is indicative of a much more complex system of disturbance mechanisms in boundary layer flows than initially expected.

A time history of total surface pressure perturbations at different streamwise positions along the cone is also presented in Fig. 12 up to 140 nose radii downstream on the cone. The upstream wavepacket at $s/R_n = 59.1$ is highly irregular and contains a multitude of forcing modes. This forcing is observed to continue decaying as the packet propagates downstream until second mode amplification is begins and exponentially amplifies the perturbation magnitudes. This second mode amplification is marked by the appearance of a more regular wavepacket at $s/R_n = 117.9$.

Fig. 13 presents the same surface perturbation time history at additional downstream locations. Again, these are non-dimensionalized by the nose radius of the cone. The y-axis scales for the figure at $s/R_n = 217.1$ and at $s/R_n = 294.3$ are not uniform with the upstream results due to the order of magnitude difference in the disturbance amplitudes. It can be seen from these results that the second mode experiences significant amplification downstream of $s/R_n = 117.8$. This surface perturbation data can be decomposed using FFT to further analyze the spectral content of the excited surface perturbations. These are presented for all of the finite pulse cases (Cases I1-I4) in Fig. 14. The preliminary LST neutral curve is also plotted in these figures as a solid black line.

Again, the finite pulse cases for all four disturbance types exhibit very similar normalized surface pressure spectra. A primary band of instabilities is observed between approximately 150-220 kHz in all four cases. This amplification occurs earliest for Case I1 (fast acoustic) and Case I3 (temperature) indicating stronger second mode responses for these cases. Furthermore, the acoustic and temperature cases (I1-I3) excite a broader band of unstable frequencies than the finite vorticity pulse (Case I4), indicating that the vorticity pulse induces a relatively weak receptivity response

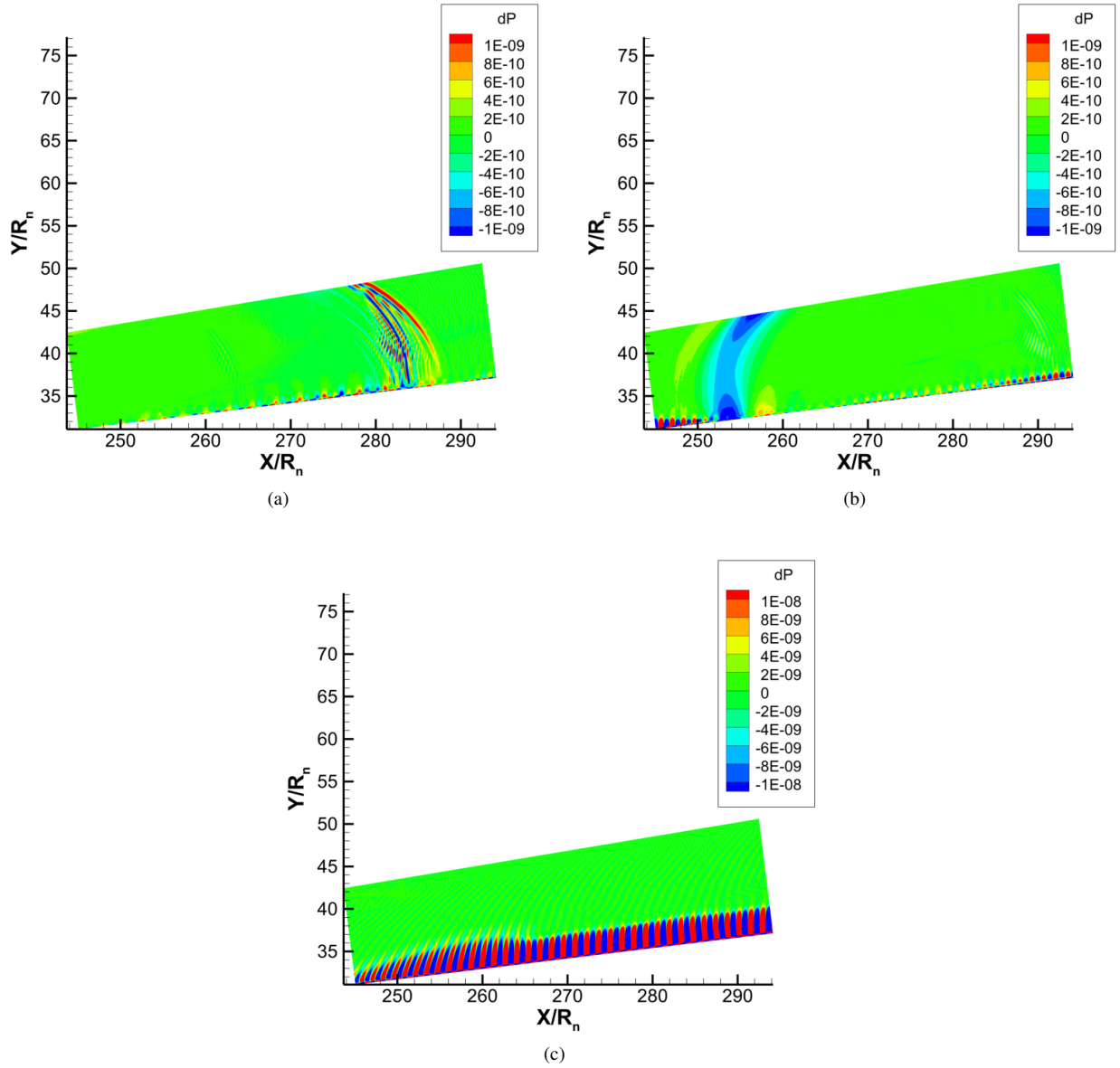

Fig. 11 Pressure snapshots in the shocklayer downstream on the cone for Case I1 for (a) Forward disturbance front, (b) Rear disturbance front, and (c) second mode disturbance.

compared to the other cases. This follows the results for the 9.525 mm case we studied previously in [36]. Significant amplification of modal instabilities was not directly observed by the unsteady DNS until approximately 150 nose radii downstream, and occurs after the swallowing distance presented by Balakumar anc Chou [21]. The preliminary LST results agree roughly with the FFT decomposed spectra, though the LST seems to predict a higher peak disturbance frequency than the DNS. This difference is attributed to nonparallel effects resulting from the nose bluntness of the geometry.

The FFT decomposed surface pressure perturbations at different streamwise locations are also presented in Fig. 15 for Cases I1 through I4 for a selection of different streamwise positions nondimensionalized by the nose radius. Again, the familiar trends are seen with an initial decay in boundary layer forcing followed by exponential modal amplification as the sampling position moves further downstream. The second mode disturbance is clearly identifiable between the frequencies of approximately 150 and 200 kHz. Very similar disturbance spectra are observed across all of the finite

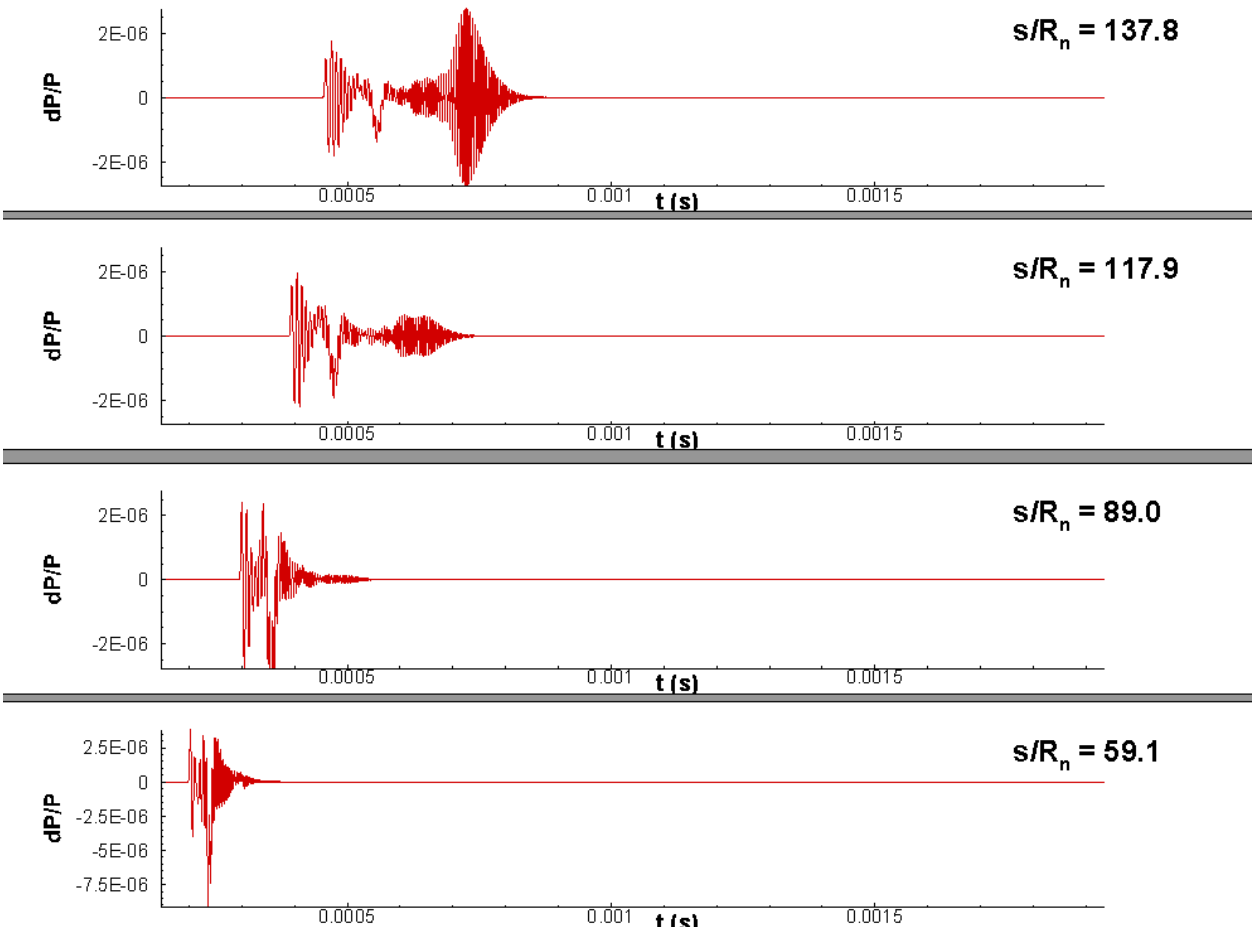

Fig. 12 Time history of normalized surface pressure perturbations resulting from Case I1 up to $s/R_n = 140$.

pulse cases. The general receptivity response of the flow to the different disturbance types can be directly observed in these surface pressure spectra. The finite temperature pulse (Case I3) was found to generate the strongest second mode and higher mode disturbances, followed by the finite fast acoustic pulse (Case I1), the finite slow acoustic pulse (Case I2), and finally the finite vorticity pulse (Case I4).

The LST phase speed and growth rate results for the 200 kHz disturbance discussed previously are used here to further verify the results of the unsteady simulations. The comparisons for Case I1, Case I2, Case I3, and Case I4 are presented in Fig. 16, 17, 18, and 19 respectively. The unsteady DNS results demonstrate good agreement with LST, and show that the finite pulses primarily generate mode F disturbances upstream on the cone in the initial shock-disturbance interaction. Furthermore, the results confirm that mode S becomes unstable after synchronization. This agrees with the general upstream receptivity mechanism observed previously in [36] and other receptivity simulations for blunt cones[9, 18] in which discrete fast acoustic disturbances are generated near the leading edge by freestream forcing. However, unlike our previous results for the 9.525 mm case in [36] the unstable second mode here is confirmed to be the discrete mode S. The unsteady signal immediately jumps to mode S after synchronization approximately 110 nose radii downstream in Fig 16, with additional modulations in the unsteady signal occurring at synchronization. While the unsteady discrete mode S destabilizes and dominates the flow beginning at this initial synchronization point, the process involves strong multimodal interactions that muddle the unsteady signal. This results in the modulated signal seen in the cases presented here.

While the primary dominant disturbances of the flow are the same for each of the unsteady pulse cases, the modal interactions resulting from different forcing can also vary somewhat. This can be directly observed in the synchronization oscillations between the cases. Similar to Case B1, Case I1 demonstrates significantly stronger modulations at the initial synchronization location, indicating stronger intermodal exchanges at this point as a result of fast acoustic forcing. This

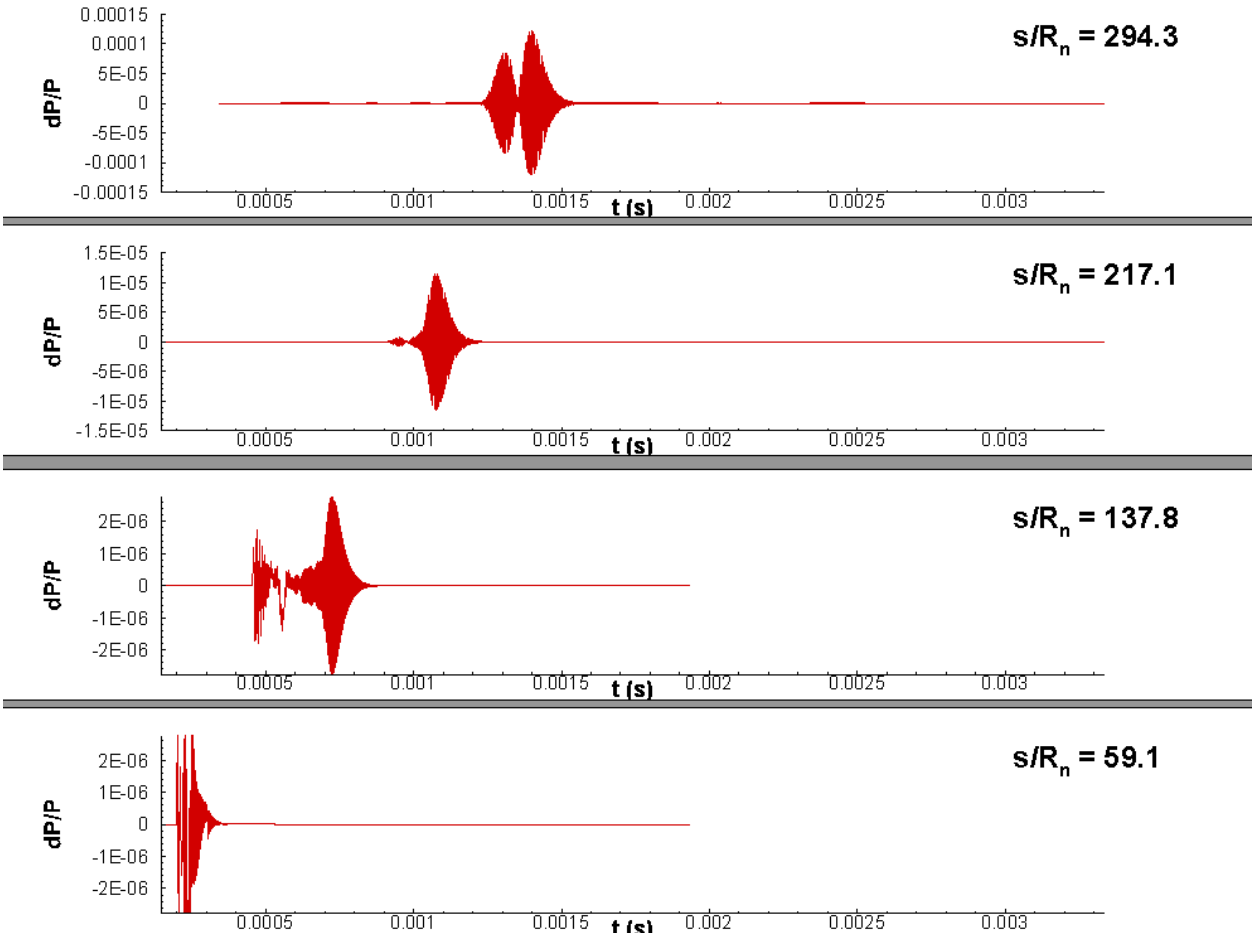

Fig. 13 Time history of normalized surface pressure perturbations resulting from Case I1.

is also reflected in the growth rate in Fig. 16b. Case I2 in Fig. 17 and Case I3 in Fig. 18 have nearly identical disturbance profiles as Case I1, though they have less pronounced modulations resulting from synchronization. This again reflects strong commonalities between the receptivity response of the temperature and slow acoustic pulses with the fast acoustic disturbance. On the other hand, Case I4 in Fig. 19 also demonstrates a different modal oscillation structure upstream of and near synchronization. The modulations for this case are much less regular and may be indicative of stronger noise components in the signal due to the relative weakness of the second mode response for freestream vorticity disturbances. This can be seen in the growth rate for Case I4 in Fig. 19b in which the signal is observed to oscillate roughly about a neutrally disturbance signal instead of solely on the mode F disturbance.

The unsteady DNS results show good agreement with the LST data, and indicate that the reduced LST analysis is able to track the primary instability development of the flow. Thus, while the LST does not take into account complicating factors such as nonparallel effects, it can still be combined with the unsteady DNS results to generate spectral receptivity coefficients for this meanflow case.

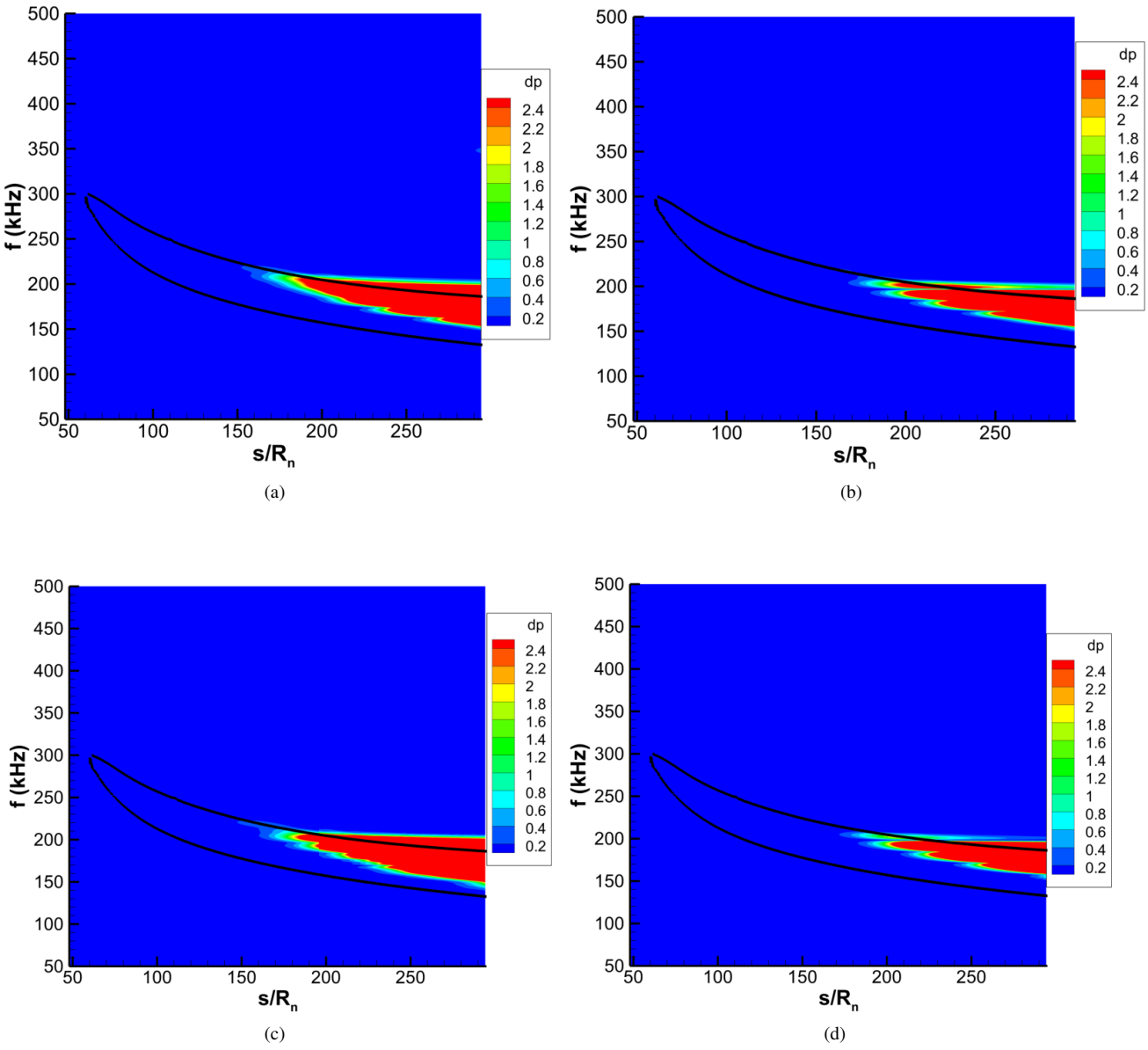

Fig. 14 Normalized FFT surface pressure contour for (a) Case I1, (b) Case I2, (c) Case I3 and (d) Case I4.

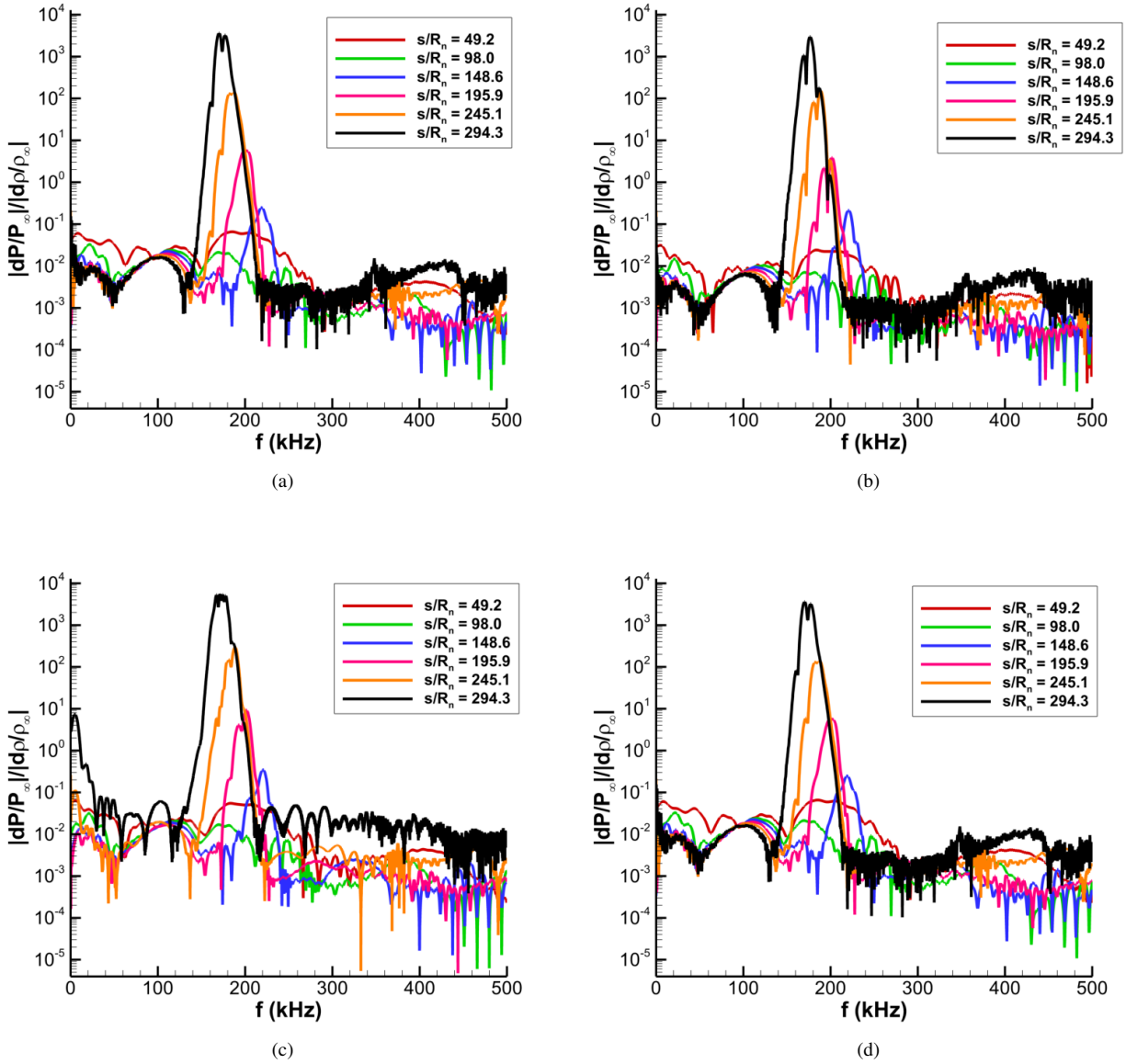

Fig. 15 FFT decomposed surface pressure spectra at various streamwise locations for (a) Case I1, (b) Case I2, (c) Case I3, and (d) Case I4.

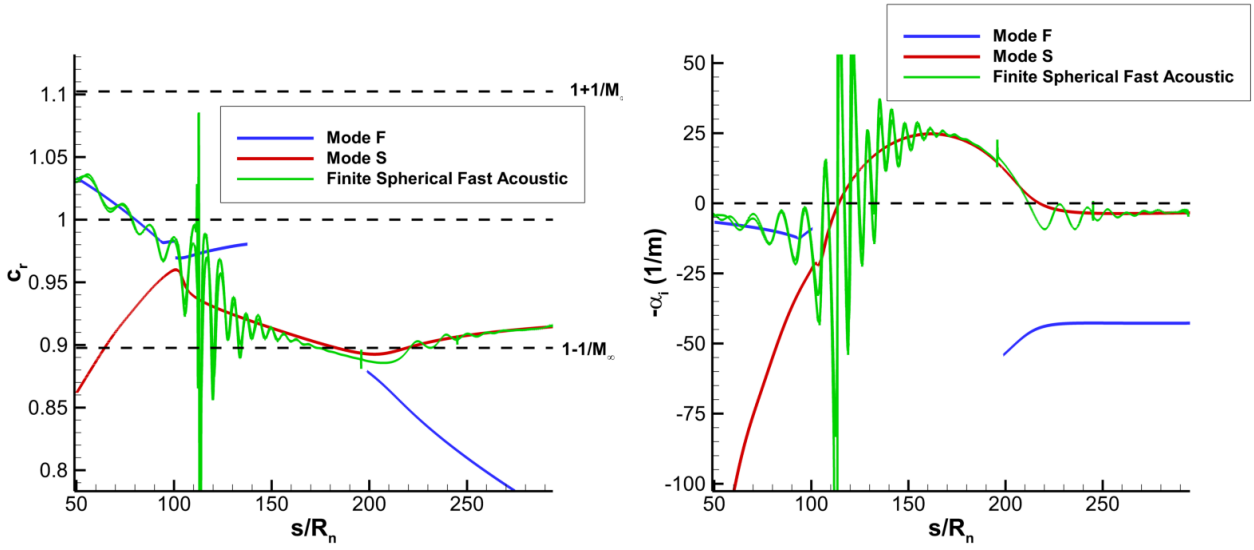

(a) (b)

Fig. 16 Case I1 unsteady DNS vs. LST predicted results for 200 kHz disturbances (a) Phase Speed (b) Growth Rate.

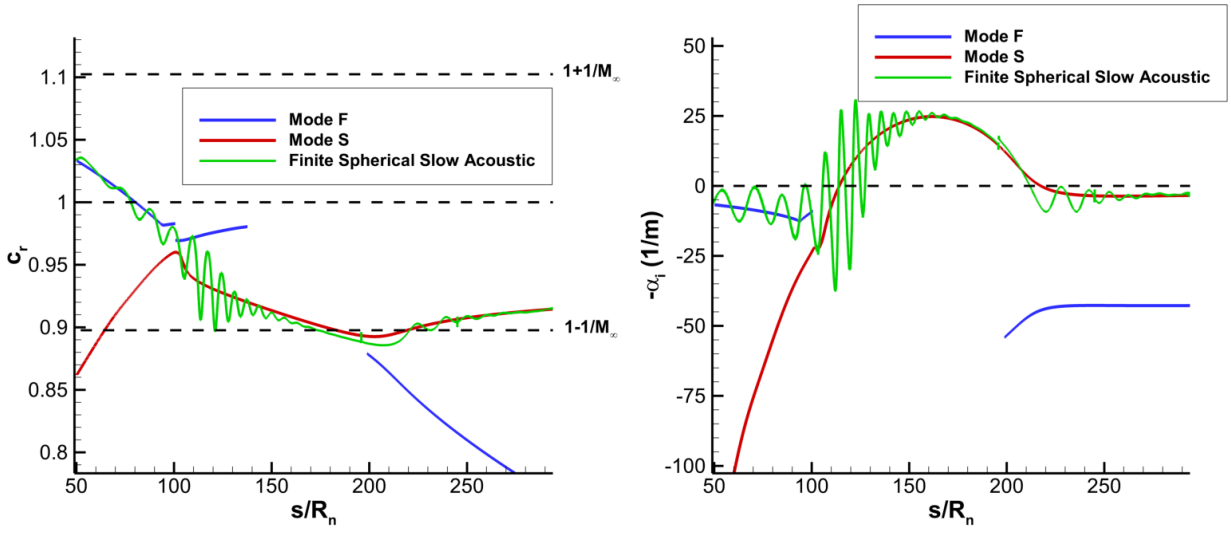

(a) (b)

Fig. 17 Case I2 unsteady DNS vs. LST predicted results for 200 kHz disturbances (a) Phase Speed (b) Growth Rate.

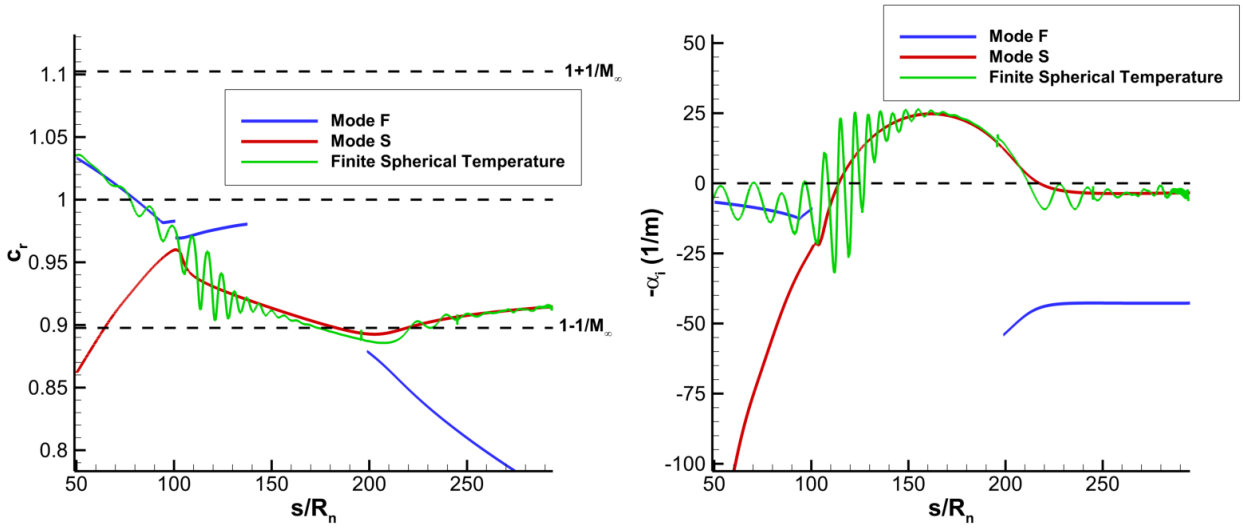

(a) (b)

Fig. 18 Case I3 DNS vs. LST predicted results for 200 kHz disturbances (a) Phase Speed (b) Growth Rate.

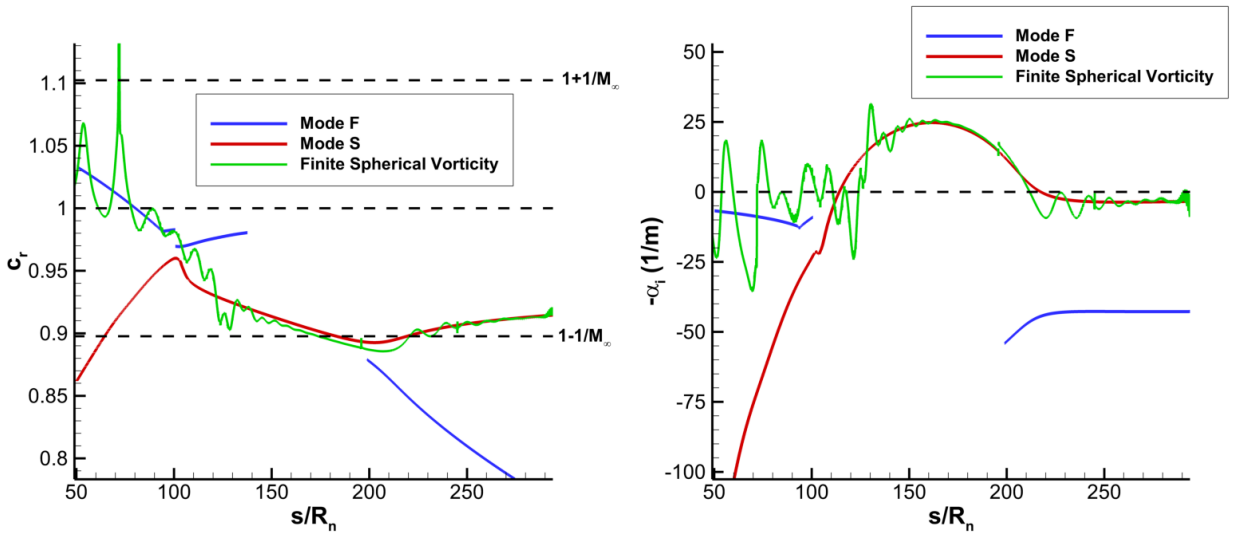

(a) (b)

Fig. 19 Case I4 DNS vs. LST predicted results for 200 kHz disturbances (a) Phase Speed (b) Growth Rate.

XI. Receptivity Results

The spectral receptivity magnitude coefficient for each of the disturbances is calculated from Eq. 42 using surface pressure perturbation data which is normalized by the freestream pulse amplitude spectra. The methodology here is the same as in our previous work [36] and is based on a method that was originally proposed by Huang and Zhong[9, 26]. The receptivity coefficients are calculated using LST-derived N-factors to extract the initial second mode amplitudes from the unsteady DNS data. Isolating the contributions of different modal disturbances to the total initial disturbance allows for greater specificity when tracking the development of instabilities across a flow domain, especially in cases with significant multimodal content.

A. Receptivity Coefficient Spectra

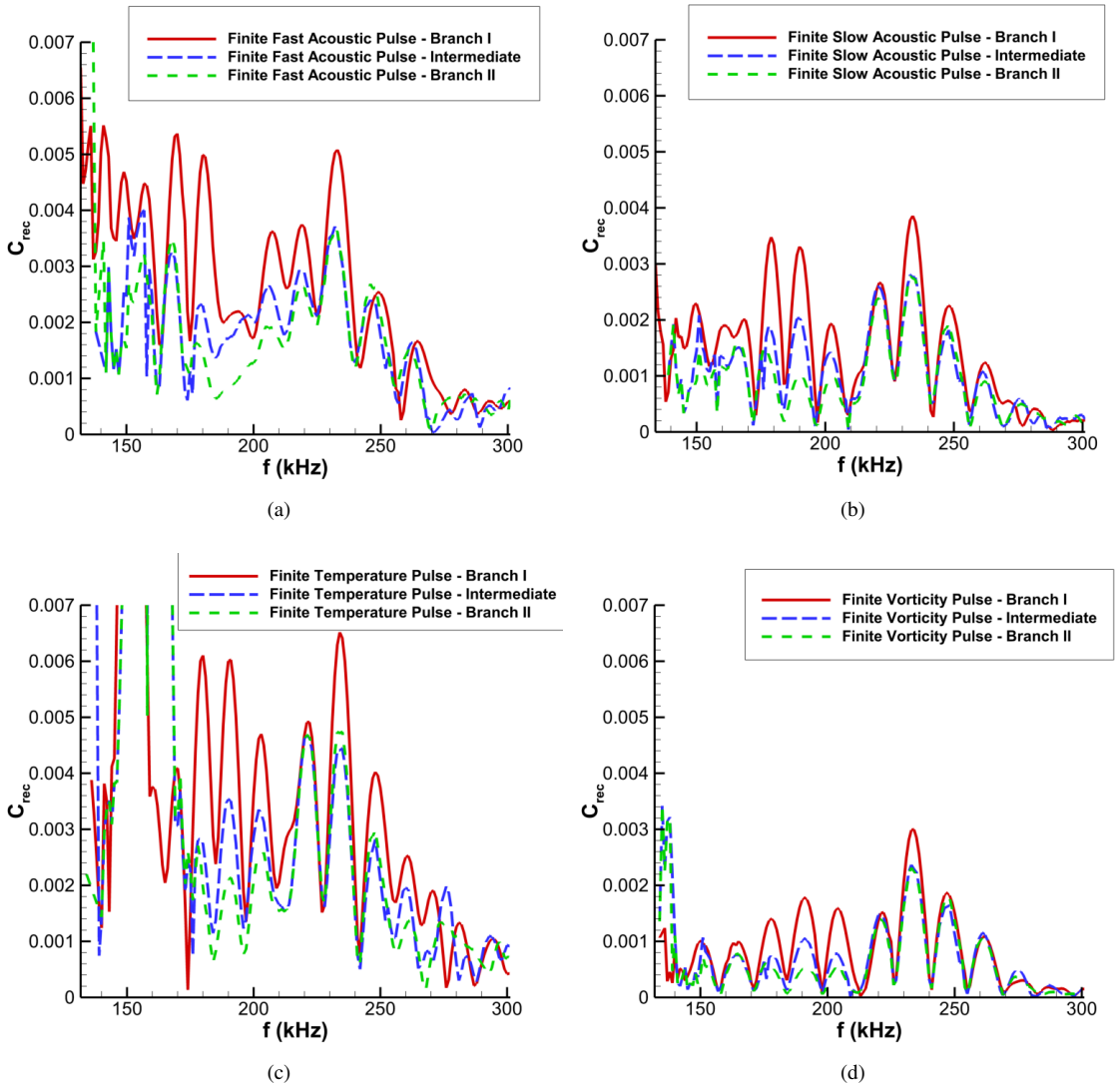

Fig. 20 Receptivity coefficients at different sampling locations for (a) Case I1, (b) Case I2, (c) Case I3, (d) Case I4.

Using Huang and Zhong's[26] method, the receptivity coefficients were calculated for each of the disturbance cases. Since these receptivity calculations may be sensitive to sampling location, a comparison of the receptivity spectra for different sampling locations was made for each of the finite spherical pulse cases. The receptivity spectra for I1-I4 at several sampling locations are presented in Fig. 20. Similar to our previous work [36], the sampling locations were

chosen to be the branch I neutral stability point x_{brI}, the branch II neutral stability point x_{brII}, and an intermediate location defined at $x_{sample} = 1.3 * x_{brI}$ for a given input disturbance frequency. These points were chosen to ensure the sampling location remained within the unstable second mode region. The branch I sampling point compares directly to conventional receptivity results reported by Balakumar and Chou[21], Kara et al.[22], Zhong and Ma[18], and Huang and Zhong[26] as the decomposition method outlined previously is not applied and the surface pressure signal is simply sampled directly. Previous work by our group showed that the complex disturbance environment generated by broadband freestream pulses resulted in larger receptivity coefficient magnitudes when the decomposition isn't applied. This was observed for both the finite and the planar pulse cases, though it was less pronounced for the finite pulses. In order to extract the initial second mode amplitudes in particular, modal decomposition was previously found to be necessary. The current comparison serves to determine if its necessity in this case as well. Fig. 20 shows the sampling point results for Cases I1-I4 and demosntrates significant second mode dominance near frequencies of 220-230 kHz. Furthermore, while the general patterns are very similar for each of the sampling locations, the branch I sampling result is shown to overpredict the receptivity coefficient by up to 80% compared to the other sampling locations. This indicates that modal decomposition is necessary to isolate the second mode in particular.

The spectral receptivity coefficients shown here are highly oscillatory, contrary to previous results seen by Huang and Zhong [26] and He and Zhong [36]. While this behavior is observed for each of the sampling locations, the degree of oscillation is reduced for the intermediate and branch II sampling cases. This is indicative of a reduction in the multimodal influence present in the results due to the decomposition method utilized here. More complex modal decomposition methods like the bi-orthogonal decomposition [46] may be able to better account for these effects.

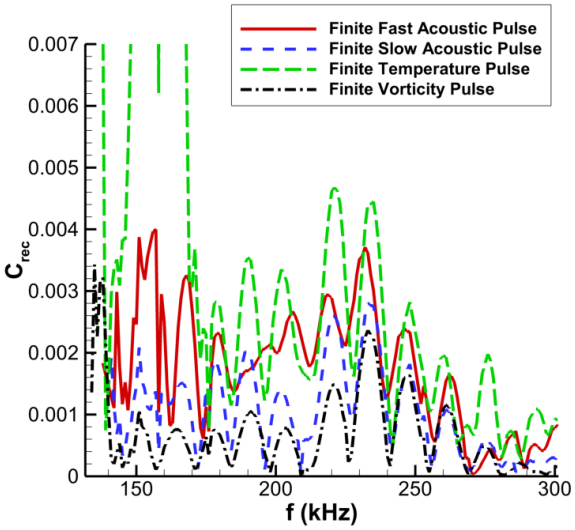

Fig. 21 Comparison of receptivity coefficient spectra for finite pulses (Cases I1-I4) using intermediate sampling location.

The total receptivity spectra for the finite spherical cases (I1-I4) are shown in Fig. 21 at the intermediate sampling location. For the finite spherical pulses studied here, it was found that the receptivity response was strongest for the temperature, fast acoustic,, slow acoustic, and vorticity disturbances in that order. Furthermore, while the receptivity coefficients here are up to two times stronger when compared to the results for the 9.525 mm nose radius Case B in [36], the vorticity coefficients are almost 8 times larger, indicating a much stronger receptivity response to vorticity disturbances for this sharper nose case.

B. Disturbance Phase Angle Spectra

The phase angle spectra for the unsteady pulse disturbance cases was also extracted from the unsteady DNS. With the data from the receptivity coefficient spectra and the phase angle spectra, the total initial receptivity response to an arbitrary axisymmetric freestream disturbance can be reconstructed[9, 23]. These initial disturbances can then be used as inputs for more advanced transition predicted methods like Mack's amplitude method[33], or to reproduce arbitrary

inlet conditions for downstream simulations studying phenomena such as nonlinear breakdown [23, 47]. The phase spectra corresponding to the magnitude coefficients presented in in the previous section are shown below in Fig. 22.

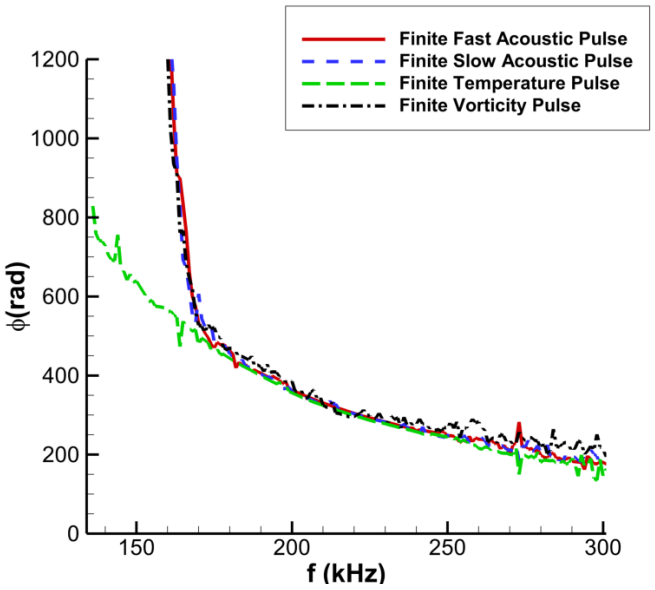

Fig. 22 Comparison of branch I phase spectra corresponding to the receptivity coefficients for cases I1-I4.

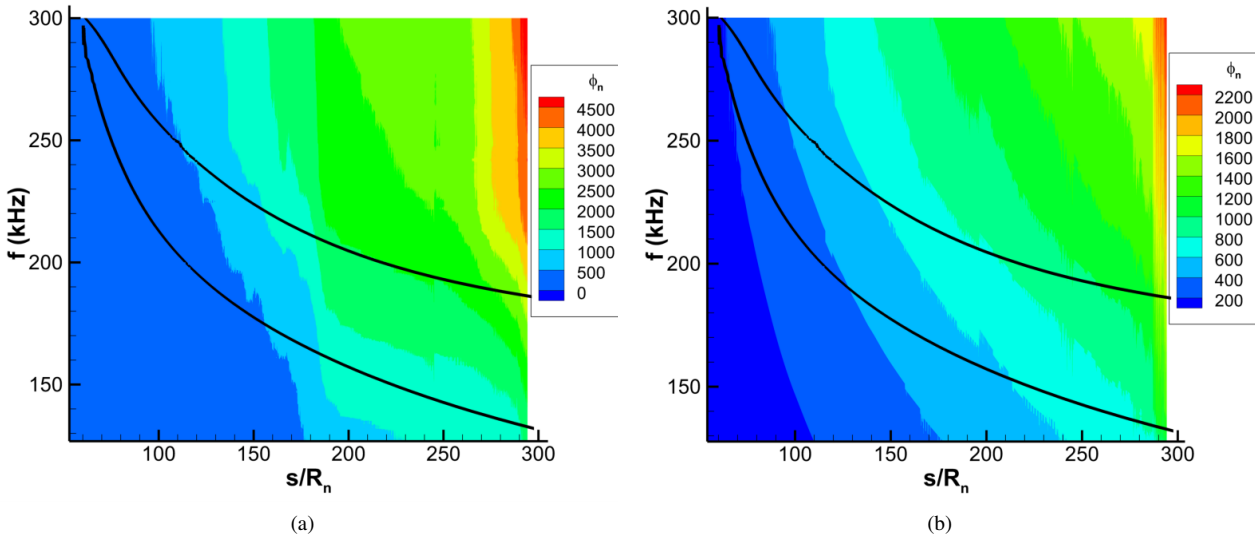

(a) (b)

Fig. 23 Phase contour and LST neutral curve for (a) Case I1 and (b) Case I3. The phase data is shifted such that it is continuous both spectrally and spatially.

The high frequency results are seen to agree very well between all four cases. Furthermore, the results for the finite fast acoustic, slow acoustic, and vorticity pulse disturbances are also very similar with each other at lower frequencies. The finite temperature pulse, on the other hand, demonstrates a different spectral phase distribution. This difference can be attributed to the differences in the disturbance phase distribution of the unsteady DNS in Fig. 23 in which the phase results are presented as a spectral contour. Similar contours for the finite slow acoustic and finite vorticity pulses (Cases

I2 and I4) were omitted for their similarity to Case I1. The presented phase results are shifted by factors of 2π such that they remain continuous both spectrally and spatially. The higher frequency disturbance phases are again observed to be very similar for the two cases. However, at lower second mode frequencies near 150 kHz we see a much more irregular gradient for Case I1. The results for Case I3, however, have a much more regular gradient throughout this low frequency region. This strong variation from the acoustic and vorticity pulses causes the dramatic variation in the lower frequency phase results observed in Fig. 22. The effects of this can be also be observed in the wavenumber for the 160 kHz disturbance shown in Fig. 24 for Cases I1 and I3 again. While the downstream and upstream behavior of the unsteady signal in both cases is very similar, near the synchronization and initial neutral stability point (at approximately $s/R_n = 200$) the signals experience significant differences in oscillation. In particular, while Case I3 experiences some multimodal oscillations at this point, the signal for Case I1 is dominated by much stronger and more densely packed oscillations. This is evidence of much stronger multimodal interference in Case I1, which is also reflected in Case I2 and I4. These phase irregularities may be caused by additional instability modes that are more readily excited by the acoustic and vorticity pulses, and may muddle the phase signal. This may include the first mode instability or supersonic mode effects, though this requires additional investigation.

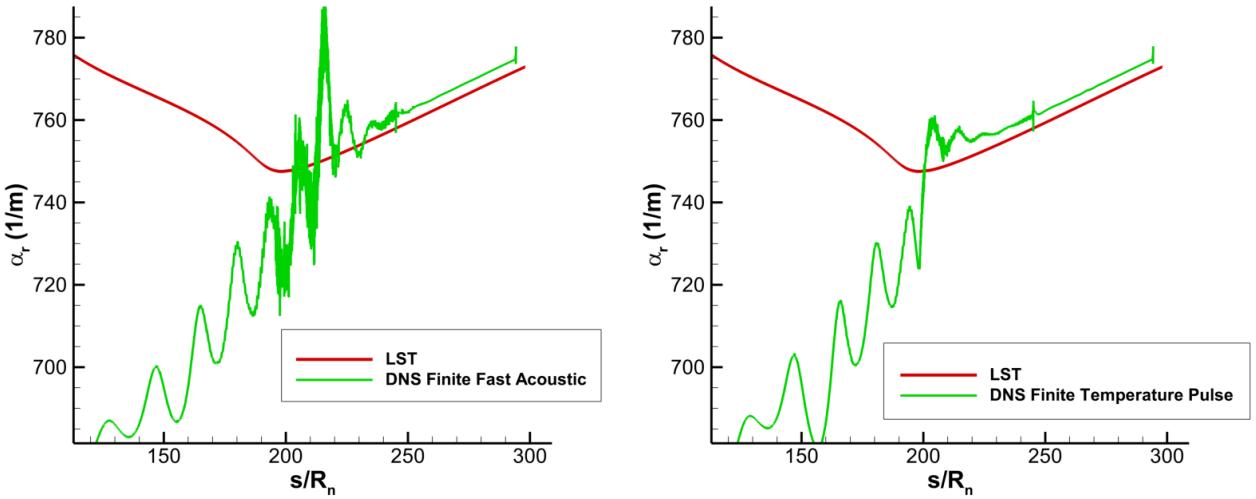

Fig. 24 Unsteady DNS vs. LST wavenumber comparison for a 160 kHz disturbance for (a) Case I1 and (b) Case I3.

XII. Conclusion

The receptivity of a 7-degree half-angle, 5.08 mm nose radius cone at mach 10 to a variety of freestream disturbances with broadband frequency spectra was investigated in this study. Spectral receptivity coefficient amplitudes and phase angles were extracted for finite spherical pulses consisting of fast acoustic, slow acoustic, temperature, and vorticity disturbances. The base flow geometry and freestream conditions were based on Marineau, et al.'s experiments[37] and the meanflow was converged using a high-order shock fitting method to solve the perfect gas Navier-Stokes equations (DNS). The stability of the meanflow was investigated using linear stability theory (LST) analysis and unsteady DNS. The pulses for unsteady DNS were modelled analytically in the freestream using Gaussian distributions to provide broadband frequency disturbances, and the shock interactions were simulated using the same high-order shock-fitting scheme as the steady DNS.

The LST analysis showed that boundary layer disturbances in a band of frequencies extending from approximately 135 kHz to 310 kHz experienced second mode growth. Furthermore, the discrete mode S emerging from the continuous slow acoustic spectrum was found to become the unstable second mode after synchronization. An entropy layer was observed beginning near the nose and the frustum, which eventually merged into the boundary layer approximately 100

nose radii downstream on the cone. Similar to Balakumar and Chou[21], LST and DNS did not predict peak second mode instability until after the entropy layer was swallowed. The N-factor in this study agrees well with Marineau et al.'s[37] PSE N-factor at the experimental transition location, with the results of this study predicting an N-factor of 3.9 vs Marineau et al.'s 3.7. The minor differences between these results is attributed to non-parallel effects that were ignored by the LST analysis utilized here, and are not believed to contribute significantly to the instability development of the flow.

The unsteady DNS simulations were decomposed into their frequency components using FFT which showed that all four of the tested freestream finite pulse disturbances generated significant second mode amplification on the cone. The finite spherical pulse cases (I1-I4) were observed to excite very similar boundary layer disturbance profiles. Due to their limited size, the finite pulses only interacted with the shock near the nose region of the cone. These isolated shock interactions allowed most of the initial broadband forcing to be damped out before second mode amplification began. The unsteady DNS results were validated against LST and showed good agreement for all of the finite pulse cases. The receptivity coefficients for the second mode disturbances were calculated by rescaling unsteady DNS pressure perturbation data with the LST N-factors. Furthermore, different sampling locations were also tested to investigate their effects on the resulting receptivity magnitude coefficients. It was again found that directly sampling the unsteady perturbation signal at the branch I neutral point overpredicts initial second mode amplitudes, as this does not account for the multimodal content of the disturbance. While the difference was not particular significant for the finite pulse cases investigated here in terms of spectral shape, the branch I sampling resulted in receptivity coefficients that were up to 80% larger than the results from other sampling locations for specific second mode disturbance frequencies. This necessitates the use of modal decomposition in order to isolate the receptivity response of the second mode in more complex flow environments. The strongest response amplitudes were observed in response to the finite temperature (Case I3), fast acoustic (Case I1), slow acoustic (Case I2), and vorticity (Case I4) pulses in that order. The spectral phase coefficients corresponding to the receptivity coefficients were also extracted for all four finite disturbance types. While the results for all four pulses agree very well at higher frequencies, the Case I3 was shown to diverge significantly from the o thers below 170 kHz. This is attributed to differences in excited disturbance content at these lower second mode frequencies between the Case I3 and the other cases, though additional investigation is still necessary to characterize this.

Additional unsteady pulse configurations remain to be studied in order to further characterize the wide envelope of potential forcing configurations. This includes more complex planar pulse disturbances, similar to what was presented in [36]. The consideration of even more complex three dimensional disturbances, such as pulses with oblique incidence, are also under consideration. Fully understanding the receptivity response of both two-dimensional and three-dimensional freestream disturbances is necessary to characterizing the general development of disturbances in hypersonic flows and improving on current transition prediciton criterion.

Acknowledgments

This research was partially supported by the Air Force Office of Scientific Research (AFOSR) under AFOSR Grant #FA9550-19-1-0206, monitored by Dr. Ivett Leyva, and by Office of Naval Research (ONR) Grant #N00014-17-1-2343, monitored by Dr. Eric Marineau. Primary computational resources were provided by Extreme Science and Engineering Discovery Environment (XSEDE) through the Texas Advanced Computing Center (TACC) and the San Diego Supercomputer Center (SDSC) under grant number TG-ASC090076, supported in part by the National Science Foundation (NSF). Additional computational support was provided by the Department of Defense High Performance Computing Modernization Program (DoD HPCMP) through project AFOSR40702004. The views and conclusions contained herein are those of the authors and should not be interpreted as necessarily representing the official policies or endorsements, either expressed or implied, of the U.S. Air Force Office of Scientific Research, Office of Naval Research, XSEDE, or the U.S. Government.

References

[1] Fedorov, A., "Transition and Stability of High-Speed Boundary Layers," *Annual Review of Fluid Mechanics*, Vol. 43, 2011, pp. 79–95. https://doi.org/10.1146/annurev-fluid-122109-160750.

[2] Reshotko, E., "Hypersonic Stability and Transition," *Hypersonic flows for reentry problems*, Vol. 1, No. A93-42576 17-02, 1991, pp. 18–34.

[3] Zhong, X., and Wang, X., "Direct Numerical Simulation on the Receptivity, Instability, and Transition of Hypersonic Boundary Layers," *Annual Review of Fluid Mechanics*, Vol. 44, 2012, pp. 527–561. https://doi.org/10.1146/annurev-fluid-120710-101208.

[4] Ma, Y., and Zhong, X., "Receptivity of a Supersonic Boundary Layer over a Flat Plate. Part 3. Effects of Different Types of Free-stream Disturbances," *Journal of Fluid Mechanics*, Vol. 532, 2005, pp. 63–109. https://doi.org/10.1017/S0022112005003836.

[5] Mack, L. M., "Boundary layer stability theory," Tech. Rep. 900-277, JPL Report, 1969.

[6] Schneider, S., "Effects of High-Speed Tunnel Noise on Laminar-Turbulent Transition," *Journal of Spacecraft and Rockets*, Vol. 38, 2001, p. 323–333. https://doi.org/10.2514/2.3705.

[7] Kovasznay, L. S. G., "Turbulence in Supersonic Flow," *Journal of the Aeronautical Sciences*, Vol. 20, No. 10, 1953, pp. 657–682. https://doi.org/10.2514/8.2793.

[8] McKenzie, J. F., and Westphal, K. O., "Interaction of Linear Waves with Oblique Shock Waves," *Physics of Fluids*, Vol. 11, No. 11, 1968, pp. 2350–2362. https://doi.org/10.1063/1.1691825.

[9] Huang, Y., and Zhong, X., "Numerical Study of Hypersonic Boundary-Layer Receptivity and Stability with Freestream Hotspot Perturbations," *AIAA Journal*, Vol. 52, No. 12, 2014, pp. 2652–2672. https://doi.org/10.2514/1.J052657.

[10] Balakumar, P., and Malik, M., "Discrete modes and continuous spectra in supersonic boundary layers," *Journal of Fluid Mechanics*, Vol. 239, 1992, pp. 631–656. https://doi.org/10.1017/S0022112092004555.

[11] Ma, Y., and Zhong, X., "Receptivity of a supersonic boundary layer over a flat plate. Part 1. Wave structures and interactions," *Journal of Fluid Mechanics*, Vol. 488, 2003, pp. 31–78. https://doi.org/10.1017/S0022112003004786.

[12] Ma, Y., and Zhong, X., "Receptivity of a supersonic boundary layer over a flat plate. Part 2. Receptivity to freestream sound," *Journal of Fluid Mechanics*, Vol. 488, 2003, pp. 79–121. https://doi.org/10.1017/S0022112003004798.

[13] Malik, M., and Balakumar, P., "Receptivity of Supersonic Boundary Layers to Acoustic Disturbances," *35th AIAA Fluid Dynamics Conference and Exhibit*, 2005. https://doi.org/10.2514/6.2005-5027.

[14] Fedorov, A. V., "Receptivity of a High-Speed Boundary Layer to Acoustic Disturbances," *Journal of Fluid Mechanics*, Vol. 491, 2003, pp. 101–129. https://doi.org/10.1017/S0022112003005263.

[15] Fedorov, A. V., Ryzhov, A. A., Soudakov, V. G., and Utyuzhnikov, S. V., "Receptivity of a high-speed boundary layer to temperature spottiness," *Journal of Fluid Mechanics*, Vol. 722, 2013, p. 533–553. https://doi.org/10.1017/jfm.2013.111.

[16] Mack, L. M., "Boundary Layer Linear Stability Theory," Tech. rep., AGARD report No. 709, 1984.

[17] Fedorov, A., and Tumin, A., "High-Speed Boundary-Layer Instability: Old Terminology and a New Framework," *AIAA Journal*, Vol. 49, No. 8, 2011, pp. 1647–1657. https://doi.org/10.2514/1.J050835.

[18] Zhong, X., and Ma, Y., "Boundary-Layer Receptivity of Mach 7.99 Flow over a Blunt Cone to Free-Stream Acoustic Waves," *Journal of Fluid Mechanics*, Vol. 556, 2006, pp. 55–103. https://doi.org/10.1017/S0022112006009293.

[19] Balakumar, P., and Kegerise, M., "Receptivity of Hypersonic Boundary Layers over Straight and Flared Cones," *48th AIAA Aerospace Sciences Meeting Including the New Horizons Forum and Aerospace Exposition*, 2010. https://doi.org/10.2514/6.2010-1065.

[20] Balakumar, P., and Kegerise, M., "Receptivity of Hypersonic Boundary Layers to Acoustic and Vortical Disturbances," *49th AIAA Aerospace Sciences Meeting including the New Horizons Forum and Aerospace Exposition*, 2011. https://doi.org/10.2514/6.2011-371.

[21] Balakumar, P., and Chou, A., "Transition Prediction in Hypersonic Boundary Layers Using Receptivity and Freestream Spectra," *AIAA Journal*, Vol. 56, No. 1, 2018, pp. 2593–2606. https://doi.org/10.2514/1.J056040.

[22] Kara, K., Balakumar, P., and Kandil, O., "Effects of Nose Bluntness on Hypersonic Boundary-Layer Receptivity and Stability over Cones," *AIAA Journal*, Vol. 55, No. 12, 2011, pp. 2593–2606. https://doi.org/10.2514/1.J050032.

[23] Lei, J., and Zhong, X., "Numerical Simulation of Freestream Waves Receptivity and Breakdown in Mach 6 Flow over Cone," *43rd Fluid Dynamics Conference*, 2013. https://doi.org/10.2514/6.2013-2741.

[24] Reshotko, E., and Tumin, A., "Role of Transient Growth in Roughness-Induced Transition," *AIAA Journal*, Vol. 42, No. 4, 2004, pp. 766–774. https://doi.org/10.2514/1.9558.

[25] Lei, J., and Zhong, X., "Linear Stability Analysis of Nose Bluntness Effects on Hypersonic Boundary Layer Transition," *Journal of Spacecraft and Rockets*, Vol. 49, No. 1, 2012, pp. 24–37. https://doi.org/10.2514/1.52616.

[26] Huang, Y., "Numerical Study of Hypersonic Boundary-Layer Receptivity and Stability with Freestream Hotspot Perturbations," Ph.D. thesis, University of California, Los Angeles, 2016.

[27] Wheaton, B., Juliano, T., Berridge, D., Chou, A., Gilbert, P., Casper, K., Steen, L., and Schneider, S., "Instability and Transition Measurements in the Mach-6 Quiet Tunnel," *39th AIAA Fluid Dynamics Conference*, 2009. https://doi.org/10.2514/6.2009-3559.

[28] Chou, A., "Characterization of Laser-Generated Perturbations and Instability Measurements on a Flared Cone," Master's thesis, Purdue University, West Lafayette, IN, 2010.

[29] Chou, A., Wheaton, B., Ward, C., Gilbert, P., Steen, L., and Schneider, S., "Instability and Transition Reserach in a Mach-6 Quiet Tunnel," *49th AIAA Aerospace Sciences Meeting*, 2011. https://doi.org/10.2514/6.2011-283.

[30] Chang, C., Malik, M., Erlebacher, G., and Hussaini, M., "Compressible stability of growing boundary layers using parabolized stability equations," *22nd Fluid Dynamics, Plasma Dynamics and Lasers Conference*, 1991. https://doi.org/10.2514/6.1991-1636, URL https://arc.aiaa.org/doi/abs/10.2514/6.1991-1636.

[31] Crouch, J., and Ng, L., "Variable N-Factor Method for Transition Prediction in Three-Dimensional Boundary Layers," *AIAA Journal*, Vol. 38, No. 2, 2000. https://doi.org/10.2514/2.973.

[32] Reed, H. L., Saric, W. S., and Arnal, D., "Linear Stability Theory Applied to Boundary Layers," *Annual Review of Fluid Mechanics*, Vol. 28, No. 1, 1996, pp. 389–428. https://doi.org/10.1146/annurev.fl.28.010196.002133.

[33] Mack, L. M., "Transition Prediction and Linear Stability Theory," Tech. rep., AGARD CP-224, 1977.

[34] Marineau, E., "Prediction Methodology for Second-Mode dominated Boundary-Layer Transition in Wind Tunnels," *AIAA Journal*, Vol. 55, No. 2, 2017. https://doi.org/10.2514/1.J055061.

[35] Ustinov, M. V., "Amplitude method of prediction of laminar-turbulent transition on a swept-wing," *Fluid Dynamics*, Vol. 52, No. 1, 2017, pp. 71–87. https://doi.org/10.1134/S0015462817010070.

[36] He, S., and Zhong, X., "Numerical Study of Hypersonic Boundary Layer Receptivity over a Blunt Cone to Freestream Pulse Disturbances," *AIAA Aviation 2020 Forum*, 2020. https://doi.org/10.2514/6.2020-2996.

[37] Marineau, E., Moraru, C., Lewis, D., Norris, J., and Lafferty, J., "Mach 10 Boundary-Layer Transition Experiments on Sharp and Blunted Cones," *19th AIAA International Space Planes and Hypersonic Systems and Technologies Conference*, 2014. https://doi.org/10.2514/6.2014-3108.

[38] Zhong, X., "High-Order Finite-Difference Schemes for Numerical Simulation of Hypersonic Boundary-Layer Transition," *Journal of Computational Physics*, Vol. 144, No. 2, 1998, pp. 662–709. https://doi.org/10.1006/jcph.1998.6010.

[39] Williamson, J., "Low-Storage Runge-Kutta Schemes," *Journal of Computational Physics*, Vol. 35, No. 1, 1980, pp. 48–56. https://doi.org/10.1016/0021-9991(80)90033-9.

[40] Malik, M. R., "Numerical Methods for Hypersonic Boundary Layer Stability," *Journal of Computational Physics*, Vol. 86, 1990, pp. 376–413. https://doi.org/10.1016/0021-9991(90)90106-B.

[41] Aleksandrova, E., Novikov, A., Utyuzhnikov, S., and Fedorov, A., "Experimental Study of the Laminar-Turbulent Transition on a Blunt Cone," *Journal of Applied Mechanics and Technical Physics*, Vol. 55, No. 3, 2014, pp. 375–385. https://doi.org/10.1134/S0021894414030018.

[42] Zhong, X., "Leading-Edge Receptivity to Free Stream Disturbance Wave for Hypersonic Flow Over a Parabola," *Journal of Fluid Mechanics*, Vol. 441, 2001, pp. 315–367. https://doi.org/10.1017/S0022112001004918.

[43] Jewell, J. S., and Kimmel, R. L., "Boundary-Layer Stabiity Analysis for Stetson's Mach 6 Blunt-Cone Experiments," *Journal of Spacecraft and Rockets*, Vol. 54, No. 1, 2017. https://doi.org/10.2514/1.A33619.

[44] Knisely, C. P., and Zhong, X., "The Supersonic Mode and the Role of Wall Temperature in Hypersonic Boundary Layers with Thermochemical Nonequilibrium Effects," *2018 Fluid Dynamics Conference*, 2018. https://doi.org/10.2514/6.2018-3218.

[45] Haley, C. L., and Zhong, X., "Mode F/S Wave Packet Interference and Acoustic-like Emissions in a Mach 8 Flow Over a Cone," *AIAA Scitech 2020 Forum*, 2020. https://doi.org/10.2514/6.2020-1579.

[46] Tumin, A., "Three-Dimensional Spatial Normal Modes in Compressible Boundary Layers," *Journal of Fluid Mechanics*, Vol. 586, 2007, pp. 295–322. https://doi.org/10.1017/S002211200700691X.

[47] Sivasubramanian, J., and Fasel, H. F., "Direct numerical simulation of transition in a sharp cone boundary layer at Mach 6: fundamental breakdown," *Journal of Fluid Mechanics*, Vol. 768, 2015, p. 175–218. https://doi.org/10.1017/jfm.2014.678.